Alma Mater Studiorum · Università di Bologna

Department of Physics and Astronomy
Bachelor Degree in Physics

Precise calibration of decay-time measurement at LHCb Upgrade I using prompt $J/\psi \to \mu^+\mu^-$

Supervisor:
Dott. Fabio Ferrari

Co-Supervisors:
Dott. Stefano Perazzini
Dott. Andrea Villa
Dott. Marco Caporale

Submitted by:
Giorgio Germano

Academic Year 2024/2025

Abstract

In this thesis, the calibration of decay-time measurements performed by the LHCb Upgrade I detector is presented. It has been performed using a prompt $J/\psi \to \mu^+\mu^-$ sample, collected during LHCb Run 3 in October 2024 and at an instantaneous luminosity of $2 \times 10^{33}\,\mathrm{cm}^{-2}\,\mathrm{s}^{-1}$.

The calibration procedure has shown that the detector measures particles decay time with a resolution

$$\sigma_{\text{eff}} = (50.4 \pm 0.3)\,\text{fs}.$$

Furthermore, it has been found that the measurements are systematically underestimated: the mean bias is

$$\delta = (-3.2 \pm 0.3)\,\text{fs}.$$

The statistical uncertainties reported are expected to be negligible compared to the systematic ones, which are currently under evaluation. Interesting and unexpected dependencies of these two quantities on various kinematic variables have been found, strong hints that the tracking system is affected by a slight misalignment of its components.

At the time of writing, this analysis is under discussion with the alignment and tracking experts of the LHCb Collaboration in order to implement the necessary corrections. The work in this thesis represents the first high-precision analysis of the calibration of decay-time measurements performed with the LHCb Upgrade I detector.

Sommario

In questa tesi è presentata la calibrazione delle misure del tempo di decadimento effettuate dal rivelatore LHCb Upgrade I, utilizzando decadimenti prompt $J/\psi \to \mu^+\mu^-$. Il campione utilizzato è stato raccolto durante il Run 3 di LHCb, nell'ottobre 2024, a una luminosità istantanea di $2 \times 10^{33}\,\mathrm{cm}^{-2}\,\mathrm{s}^{-1}$.

La procedura di calibrazione ha evidenziato che il rivelatore è in grado di misurare il tempo di decadimento delle particelle con una risoluzione

$$\sigma_{\text{eff}} = (50.4 \pm 0.3)\,\text{fs}.$$

È stato inoltre osservato che la misura è sistematicamente sottostimata: in media, il bias è

$$\delta = (-3.2 \pm 0.3)\,\text{fs}.$$

Ci si aspetta che gli errori statistici riportati siano trascurabili rispetto a quelli sistematici, che sono in fase di valutazione. Inoltre, sono state trovate interessanti e inaspettate dipendenze di queste due quantità da diverse variabili cinematiche, forti indizi del fatto che il sistema di tracciamento sia affetto da un leggero disallineamento delle sue componenti.

Al momento della scrittura di questa tesi, lo studio è in fase di discussione con gli esperti di allineamento e ricostruzione dell'esperimento per implementare le opportune correzioni. Il lavoro contenuto in questa tesi rappresenta il primo studio ad altissima precisione per la calibrazione della misura del tempo di decadimento effettuata con il rivelatore LHCb Upgrade I.

Contents

Introduction

One of the biggest open questions in modern particle physics is finding an explanation for the *baryonic asymmetry*: in the observable Universe, matter is predominant with respect to antimatter. As their contact results in annihilation, the existence of our Universe would be impossible if this asymmetry did not occur.

Matter and antimatter are linked by the $\mathcal{CP}$ transformation, the composition of the inversion of all internal charges $\mathcal{C}$, and the inversion of parity (the flip in the sign of spatial coordinates) $\mathcal{P}$. The baryonic asymmetry, thus, can be seen from a $\mathcal{CP}$-symmetry violation point of view. To the present day, all the $\mathcal{CP}$-violation measurements fail to explain this asymmetry.

The LHCb experiment at CERN is specialized in the measurement of $\mathcal{CP}$ violation in the heavy-quark sector, analysing processes that break this symmetry. Since it began taking data in 2010, LHCb has brought many interesting results and world-leading measurements. The detector underwent a major upgrade, the LHCb Upgrade I, between 2018 and 2022. Its almost complete renewal made it possible to operate it at five times higher instantaneous luminosity during Run 3.

The precise determination of the decay time of B mesons is crucial for the LHCb physics program. Bias and resolution effects have substantial consequences on the measurements of $\mathcal{CP}$-violation parameters, causing errors and dilutions that are non-negligible. The larger datasets expected with the LHCb Upgrade call for a very precise calibration of these effects.

This work is divided into three parts:

- The first chapter introduces the theoretical framework of the Standard Model with a major focus on the CKM matrix, which describes flavour mixing and $\mathcal{CP}$ violation in weak interactions. The concept of the unitarity triangle is introduced as a geometric representation of CKM unitarity conditions, and the different mechanisms of $\mathcal{CP}$ violation, direct, indirect (via neutral meson oscillation), and in the interference between the two, are explained, particularly in the context of neutral B mesons.

- The second chapter provides an overview of the LHCb Upgrade I detector at CERN, optimized for studying $\mathcal{CP}$ violation in heavy-flavour hadrons. The chapter details its main subsystems: tracking (VELO, UT, SciFi, magnet), particle identification (RICH detectors, calorimeters, and muon system), and the two-stage trigger system (HLT1 and HLT2).

- The last chapter focuses on data-driven analysis of prompt $J/\psi \to \mu^+\mu^-$ decays to calibrate the decay-time bias and resolution. After a study of the effects that an imperfect decay-time measurement has on the determination of $\mathcal{CP}$-violation parameters, and a

justification of the choice of the data sample, the fitting strategy is presented. The analysis has been performed first by subtracting the contribution of combinatorial background, then by binning the sample according to seven different variables. Fits to the decay-time distribution of each subsample are then performed to extract the calibration of the decay-time bias and resolution. Finally, the dependences of the bias, resolution and other quantities on the binning variables are analyzed.

Chapter 1

The Standard Model

1.1 Fundamental particles and interactions

The Standard Model (SM) is a theoretical framework that describes three of the four currently known fundamental interactions: electromagnetism, weak and strong interaction, but not gravity. The SM is a quantum field theory that describes fundamental particles as quantized excitations of fundamental fields.

Many SM predictions have been experimentally confirmed with utmost precision. Nevertheless, like every physical theory, the SM has some limitations, and some *Beyond the Standard Model* (BSM) processes have been observed[1]. Studying and explaining those is one of the main currently open problems in physics.

1.1.1 Spin-statistics theorem

A first classification of the fundamental particles described by the SM can be made by their *spin*. Spin is often related to the classical, macroscopic quantity *spin angular momentum*. However, this analogy is misleading, as spin is a fundamental property of quantum particles (like mass and electrical charge, for example), and linking it to the rotation of the particle around its own centre of mass leads to unsurmountable contradictions[2].

The spin-statistic theorem, an important result proven by Pauli and his student Fierz around 1940, affirms [3] that the states of two identical particles (not necessarily fundamental) are

- *symmetric* under the interchange of the particles, if their spin is integer;
- *anti-symmetric* under the interchange of the particles, if their spin is half-integer.

It can be shown that the first kind of particles follows Bose-Einstein statistics and are thus called **bosons**, whereas the latter obey Fermi-Dirac statistics and are referred to as **fermions**. Every fundamental particle is either a fermion or a boson.

[1] For example, neutrino flavour oscillations are not predicted by the SM and yet have been observed. They were first discovered by the Super-Kamiokande collaboration in 1998 [1].

[2] Pauli showed that, if we assume the electron to be a sphere with radius equal to the electron classical radius $r_e = \frac{1}{4\pi\varepsilon_0}\frac{e^2}{m_e c^2} \approx 3\,\text{fm}$, in order to have the observed magnetic momentum $\mu = (1.001\,159\,652\,180\,59 \pm 0.000\,000\,000\,000\,13)\ \mu_B$ [2], its surface should rotate faster than the speed of light, violating relativity.

1.1.2 Bosons and interactions

The *force carriers*, mediators of the three interactions described by the SM, are bosons. It is important to note that the mediators themselves can be affected by the very interaction they carry.

The SM is a gauge theory described by the symmetry group

$$SU(3)_C \otimes SU(2)_L \otimes U(1)_Y$$

where $SU(3)_C$ describes the strong interaction, while $SU(2)_L \otimes U(1)_Y$ are the chiral weak and the hypercharge group. The electromagnetic interaction $U(1)_{EM}$ and weak interaction $SU(2)_W$ that we observe are the result of spontaneous symmetry breaking of $SU(2)_L$ and $U(1)_Y$ due to the Higgs mechanism, as described by Glashow, Weinberg and Salam [4, 5, 6].

Particles are affected by one of these forces only if they possess the corresponding *gauge charge*: colour charge, weak isospin and electromagnetic charge. An *antiparticle* has the same mass as its associated particle, but has every internal charge inverted.

The particles mediating fundamental interactions are:

- **Gluons** ($g_1, \dots g_8$), for strong interaction. $SU(3)$ is a Lie group with $3^2 - 1 = 8$ dimensions; thus, there are 8 particles which mediate this interaction. Gluons are considered massless and have no electric charge, but they do possess colour charge and thus interact via strong interaction (for this reason, they are called *self-interacting*). Strong interaction becomes more intense as the distance increases: despite its mediators being massless, it is not a long-range interaction, and its range is ~ 1 fm.

- **Bosons** W^+, W^- and Z^0, for weak interaction. In a similar manner, there are $2^2 - 1 = 3$ mediators. These particles have masses of $\sim 100\,\mathrm{GeV}/c^2$ and are thus short-lived, making the weak interaction's range even smaller than the strong one ($\sim 10 \times 10^{-18}$ m). W^+ and W^- have electric charge and are self-interacting.

- **Photons** (γ), for electromagnetic interaction. They are massless (making the electromagnetic interaction a long-distance interaction, with infinite range) and with no electric charge, thus photons are not self-interacting.

All the 12 aforementioned force mediators have spin equal to 1. In addition to these fundamental fields, there is the **Higgs boson**, a particle with spin 0. The Higgs field is responsible for the mass of particles and for making the gauge charges of the weak and electromagnetic interactions interdependent.

1.1.3 Fermions

Fermions can be further classified depending on the interactions[3] that act on them. Any fermion undergoes weak interaction; however:

[3]Every particle with a mass interacts gravitationally, but, as previously said, the SM does not explain this interaction. A gravitational force carrier has been hypothesized, the *graviton*, which is expected to be massless and with spin 2. However, there is currently no experimental evidence of its existence.

- **Leptons** do not interact strongly. There are 6 different types, or *flavours*, of leptons (and 6 anti-leptons): three *electron-like* leptons (e^-, μ^- and τ^-) and three *neutrinos* (ν_e, ν_μ and ν_τ). Leptons can be grouped in isospin doublets, also called *generations*:

$$\begin{pmatrix}\nu_e\\ e^-\end{pmatrix} \qquad \begin{pmatrix}\nu_\mu\\ \mu^-\end{pmatrix} \qquad \begin{pmatrix}\nu_\tau\\ \tau^-\end{pmatrix}$$

  The first element of each generation has weak-isospin projection $T_3 = +\frac{1}{2}$, while the second one has $T_3 = -\frac{1}{2}$. Electron-like leptons have a negative unitary electric charge, while neutrinos, are their name suggests, are neutral. All leptons have weak hypercharge $Y_W = -1$, which relates to electric charge Q and weak-isospin projection via the Gell-Mann–Nishijima formula [7]

$$Y_W = 2(Q - T_3)$$

  .

- **Quarks** interact via strong interaction. Similarly to leptons, there are six flavours of quarks: three *up-like* quarks (up u, charm c and top t) and three *down-like* ones (down d, strange s and beauty b), that can be arranged in generations:

$$\begin{pmatrix}u\\ d\end{pmatrix} \qquad \begin{pmatrix}c\\ s\end{pmatrix} \qquad \begin{pmatrix}t\\ b\end{pmatrix}$$

  All up-like quarks have $Q = +\frac{2}{3}$, while down-like have $Q = -\frac{1}{3}$.

Quarks (q) have colour charge, which can be red, green or blue; anti-quarks ($\bar{q}$) can be anti-red, anti-green or anti-blue. As stated in Sec. 1.1.2, this interaction grows stronger as distance increases; for this reason, quarks have only been observed in bound states, called **hadrons**. These states, in order to have a neutral colour charge, usually are in the $q\bar{q}$ form (**mesons**), where (anti-)quarks have opposite colour charge, or in the form qqq (**baryons**), where each quark has a different colour charge (or $\bar{q}\bar{q}\bar{q}$, antibaryons). Other exotic combinations of quarks, tetraquarks ($q\bar{q}q\bar{q}$) and pentaquarks ($qqqq\bar{q}$ or $\bar{q}\bar{q}\bar{q}\bar{q}q$), have been observed [8, 9]. See Fig. 1.1 for a scheme of the SM fundamental particles.

1.2 CKM matrix

1.2.1 Flavour mixing

The weak interaction has two interesting and unique properties: it affects every quark and lepton, and it is the only fundamental interaction that does not preserve flavour. This means that, in a weakly-mediated decay, the final number of particles with a specific flavour can be different from the initial one.

Cabibbo, and later Kobayashi and Maskawa, proposed [10, 11] a model of *universal weak interaction*, in which the coupling, and thus the intensity of the interaction, is the same for leptons and quarks. In addition to that, the former are eigenstates of the interactions, while the latter are not. In other words, the mass eigenstates of strong interaction corresponding to

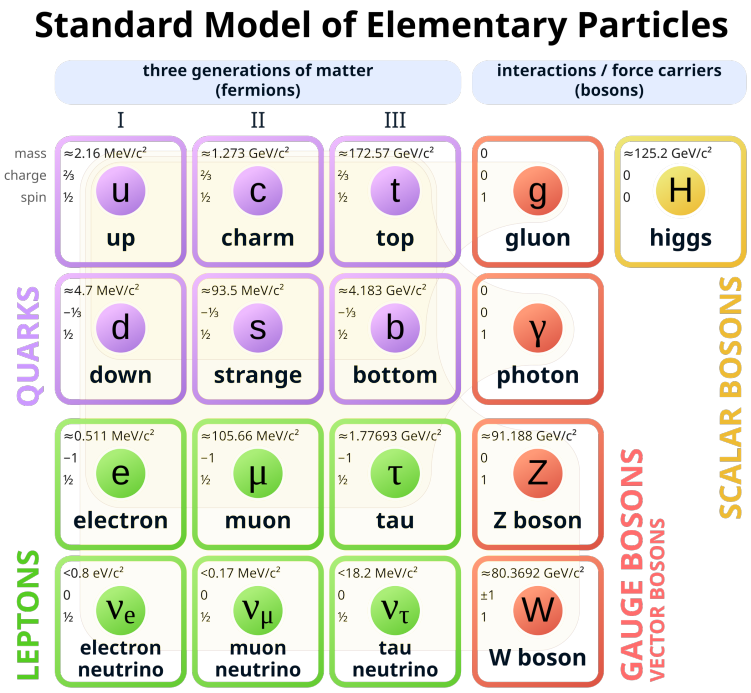

Figure 1.1: Fundamental particles of the SM.

down-like[4] quarks ($|d\rangle$, $|s\rangle$, $|b\rangle$) are rotated by a certain angle with respect to the eigenstates of weak interaction (which we denote $|d'\rangle$, $|s'\rangle$, $|b'\rangle$).

We can think of this rotation as a unitary endomorphism of the eigenstates space, and thus represent it with a unitary 3×3 matrix, the CKM matrix:

$$\begin{pmatrix} d' \\ s' \\ b' \end{pmatrix} = \begin{pmatrix} V_{ud} & V_{us} & V_{ub} \\ V_{cd} & V_{cs} & V_{cb} \\ V_{td} & V_{ts} & V_{tb} \end{pmatrix} \begin{pmatrix} d \\ s \\ b \end{pmatrix} = V_{\text{CKM}} \begin{pmatrix} d \\ s \\ b \end{pmatrix} . \tag{1.1}$$

1.2.2 V_{CKM} parametrization

A generic $N \times N$ complex matrix can be described with N^2 complex numbers and thus $2N^2$ real numbers. The CKM matrix, however, has some properties which reduce its number of free parameters:

- Unitarity: given that $\sum_k V_{ki} {V_{kj}}^* = \delta_{ij}$, we have N constraints for the diagonal elements and $N^2 - N$ for the off-diagonal ones;

- Freedom of the relative quark phases: the relative phase of each quark can vary freely. When this happens, the CKM matrix is modified by means of fully diagonal matrices containing the relative quark phases multiplying it. When all the relative phases equal

[4] By convention, the eigenstates corresponding to down-like quarks are rotated, but the up-like ones could be rotated instead.

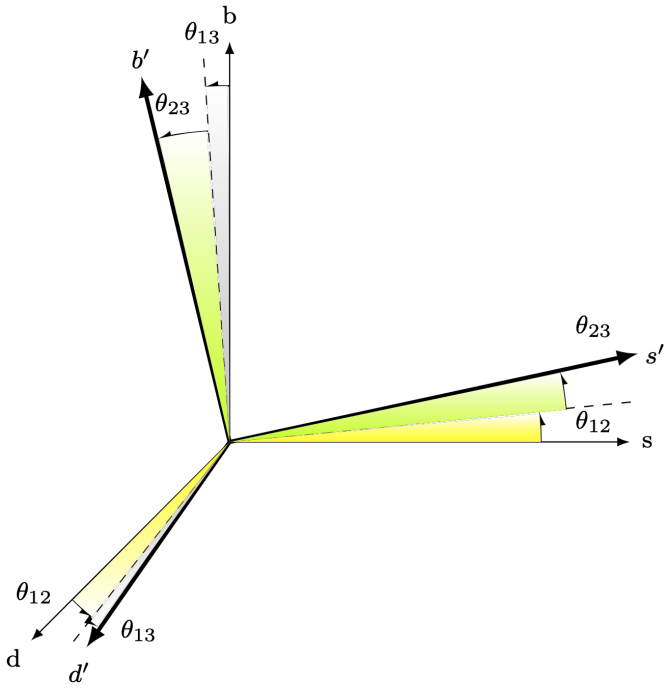

Figure 1.2: Illustration of the three Euler angles in the eigenstate space.

each other, no effect is observed, since the overall phase has no effect on the observed phenomenology. This means that for an $N \times N$ matrix, $2N$ phases are present, one for each quark, and from these $2N - 1$ are redundant and can be removed.

Thus, a matrix with these properties has $2N^2 - (N^2 - N) - N - (2N - 1) = (N - 1)^2$ free parameters. The CKM matrix, having $N = 3$, can be described with 4 real numbers. Three of these parameters are *Euler angles* (see Fig. 1.2), describing the rotations among the three directions; the last one is generically referred to as *complex phase*.

Many parametrizations of the CKM matrix are possible; a standard convention has become [12]

$$
\begin{aligned}
V_{\mathrm{CKM}} &= \begin{pmatrix} 1 & 0 & 0 \\ 0 & c_{23} & s_{23} \\ 0 & -s_{23} & c_{23} \end{pmatrix} \begin{pmatrix} c_{13} & 0 & s_{13}e^{-i\delta} \\ 0 & 1 & 0 \\ -s_{13}e^{i\delta} & 0 & c_{13} \end{pmatrix} \begin{pmatrix} c_{12} & s_{12} & 0 \\ -s_{12} & c_{12} & 0 \\ 0 & 0 & 1 \end{pmatrix} \\
&= \begin{pmatrix} c_{12}c_{13} & s_{12}c_{13} & s_{13}e^{-i\delta} \\ -s_{12}c_{23} - c_{12}s_{23}s_{13}e^{i\delta} & c_{12}c_{23} - s_{12}s_{23}s_{13}e^{i\delta} & s_{23}c_{13} \\ s_{12}s_{23} - c_{12}c_{23}s_{13}e^{i\delta} & -c_{12}s_{23} - s_{12}c_{23}s_{13}e^{i\delta} & c_{23}c_{13} \end{pmatrix},
\end{aligned} \tag{1.2}
$$

where $s_{ij} = \sin\theta_{ij}$ and $c_{ij} = \cos\theta_{ij}$. The three Euler angles θ_{12}, θ_{23} and θ_{13} are called *mixing angles*; the complex phase δ is responsible for $\mathcal{CP}$ violation (see Sec. 1.3). It is important to notice that the SM does not offer theoretical predictions about these parameters: they can only be experimentally measured.

Experiments have shown that $s_{13} \ll s_{23} \ll s_{12} \ll 1$ [13]. It is thus convenient to represent V_{CKM} using the so-called Wolfenstein parametrization [14]:

$$s_{12} = \lambda = \frac{|V_{us}|}{\sqrt{|V_{ud}|^2 + |V_{us}|^2}}, \tag{1.3}$$

$$s_{23} = A\lambda^2 = \lambda \left| \frac{V_{cb}}{V_{us}} \right|, \tag{1.4}$$

$$s_{13} e^{i\delta} = V_{ub}^* = A\lambda^3(\rho + i\eta) = \frac{A\lambda^3(\bar{\rho} + i\bar{\eta})\sqrt{1 - A^2\lambda^4}}{\sqrt{1 - \lambda^2}\left[1 - A^2\lambda^4(\bar{\rho} + i\bar{\eta})\right]}, \tag{1.5}$$

and V_{CKM} can be written up to $\mathcal{O}(\lambda^4)$ in terms of λ, A, ρ and η:

$$V_{\text{CKM}} = \begin{pmatrix} 1 - \lambda^2/2 & \lambda & A\lambda^3(\rho - i\eta) \\ -\lambda & 1 - \lambda^2/2 & A\lambda^2 \\ A\lambda^3(1 - \rho - i\eta) & -A\lambda^2 & 1 \end{pmatrix} + \mathcal{O}(\lambda^4), \tag{1.6}$$

that, being $\lambda \approx 0.22$ [13], shows a hierarchy in flavour mixing, as

$$V_{\text{CKM}} \sim \begin{pmatrix} 1 & \lambda & \lambda^3 \\ \lambda & 1 & \lambda^2 \\ \lambda^3 & \lambda^2 & 1 \end{pmatrix}.$$

The Wolfenstein parametrization ensures that V_{CKM} is unitary up to $\mathcal{O}(\lambda^4)$. In fact, by directly computing its inverse we find that

$${V_{\text{CKM}}}^{-1} = \begin{pmatrix} 1 - \lambda^2/2 & -\lambda & A\lambda^3(1 - \rho + i\eta) \\ \lambda & 1 - \lambda^2/2 & -A\lambda^2 \\ A\lambda^3(\rho + i\eta) & A\lambda^2 & 1 \end{pmatrix} + \mathcal{O}(\lambda^4) \approx {V_{\text{CKM}}}^{\dagger}.$$

1.2.3 The unitarity triangle

It's interesting to find the physical meaning of the unitarity condition of V_{CKM} (as defined in Eq. (1.1)).

The three *unitarity relations*

$$\sum_{i=d,s,b} V_{ui} {V_{ui}}^* = 1,$$
$$\sum_{i=d,s,b} V_{ci} {V_{ci}}^* = 1,$$
$$\sum_{i=d,s,b} V_{ti} {V_{ti}}^* = 1,$$

tell us that the sum of the squared moduli of the coupling to down-like quarks is the same for all up-like ones, a property called *weak universality*.

From the unitary condition we also have six *orthogonality relations*

$$\sum_{i=d,s,b} V_{ui} {V_{ci}}^* = 0 \qquad \sum_{i=d,s,b} V_{ui} {V_{ti}}^* = 0 \qquad \sum_{i=d,s,b} V_{ci} {V_{ti}}^* = 0 \tag{1.7}$$

and

$$\sum_{j=u,c,t} V_{jd}{}^{*}V_{js} = 0 \qquad \boxed{\sum_{j=u,c,t} V_{jb}{}^{*}V_{jd} = 0} \qquad \sum_{j=u,c,t} V_{jb}{}^{*}V_{js} = 0. \tag{1.8}$$

Eq. (1.7) and (1.8) are basically sums of complex numbers that sum up to 0, and can thus be represented by triangles in the complex plane.

However, some of the orthogonality relations contain terms with different powers of λ, meaning that their corresponding triangles are almost degenerate. For instance, the first condition in (1.7) is

$$\sum_{i=d,s,b} V_{ui}V_{ci}{}^{*} = \underbrace{V_{ud}V_{cd}{}^{*}}_{\mathcal{O}(\lambda)} + \underbrace{V_{us}V_{cs}{}^{*}}_{\mathcal{O}(\lambda)} + \underbrace{V_{ub}V_{cb}{}^{*}}_{\mathcal{O}(\lambda^5)} = 0.$$

Only two of the six orthogonality relations are homogeneous in λ (those highlighted in Eq. (1.7) and (1.8)):

$$\sum_{i=d,s,b} V_{ui}V_{ti}{}^{*} = \underbrace{V_{ud}V_{td}{}^{*}}_{\mathcal{O}(\lambda^3)} + \underbrace{V_{us}V_{ts}{}^{*}}_{\mathcal{O}(\lambda^3)} + \underbrace{V_{tb}V_{ub}{}^{*}}_{\mathcal{O}(\lambda^3)} = 0 \tag{1.9}$$

and

$$\sum_{j=u,c,t} V_{jb}{}^{*}V_{jd} = \underbrace{V_{ud}V_{ub}{}^{*}}_{\mathcal{O}(\lambda^3)} + \underbrace{V_{cd}V_{cb}{}^{*}}_{\mathcal{O}(\lambda^3)} + \underbrace{V_{td}V_{tb}{}^{*}}_{\mathcal{O}(\lambda^3)} = 0. \tag{1.10}$$

The triangle given by Eq. (1.10) is often referred to as *the* (CKM) unitarity triangle. If we divide each side by $|V_{cd}V_{cb}|$ and rotate the triangle (i. e. without changing the relative angles), we get a triangle with vertices in (0,0) (1,1) and $(\bar{\rho}, i\bar{\eta})$, as seen in Fig. 1.3a, where

$$\bar{\rho} + i\bar{\eta} \equiv \frac{V_{ud}V_{ub}{}^{*}}{V_{cd}V_{cb}{}^{*}}. \tag{1.11}$$

Substituting the components of V_{CKM} of Eq. (1.6) into Eq. (1.11) we get

$$\begin{cases} \bar{\rho} = \rho(1-\lambda^2/2) + \mathcal{O}(\lambda^4) \\ \bar{\eta} = \eta(1-\lambda^2/2) + \mathcal{O}(\lambda^4) \end{cases}$$

which is consistent with the definitions of $\bar{\rho}$, $\bar{\eta}$ of Eq. (1.5). The unitarity triangle defines three angles:

$$\beta \equiv \arg\left(-\frac{V_{cd}V_{cb}{}^{*}}{V_{td}V_{tb}{}^{*}}\right), \qquad \alpha \equiv \arg\left(-\frac{V_{td}V_{tb}{}^{*}}{V_{ud}V_{ub}{}^{*}}\right), \qquad \gamma \equiv \arg\left(-\frac{V_{ud}V_{ub}{}^{*}}{V_{cd}V_{cb}{}^{*}}\right).$$

These angles, as well as other parameters[5], are quantities that can be measured to constrain the unitarity triangle, as can be seen in Figs. 1.4 and 1.5.

As of April 2024, the experimental values of the elements of V_{CKM} are [13]:

$$V_{\text{CKM}} = \begin{pmatrix} 0.97435 \pm 0.00016 & 0.22501 \pm 0.00068 & 0.003732^{+0.000090}_{-0.000085} \\ 0.22487 \pm 0.00068 & 0.97349 \pm 0.00016 & 0.04183^{+0.00079}_{-0.00069} \\ 0.00858^{+0.00019}_{-0.00017} & 0.04111^{+0.00077}_{-0.00068} & 0.999118^{+0.00029}_{-0.00034} \end{pmatrix}.$$

[5]Other parameters are $\varepsilon_K = (0.002\,227 \pm 0.000\,014)$, the $\mathcal{CP}$ violation in $K^0 - \bar{K}^0$ mixing; $\Delta m_{B^0} = (0.5065 \pm 0.0019)\,\text{ps}^{-1}$ and $\Delta m_{B_s^0} = (17.741 \pm 0.020)\,\text{ps}^{-1}$, parameters associated to the oscillations between, respectively, $B^0 \leftrightarrow \overline{B}^0$ and $B_s^0 \leftrightarrow \overline{B}_s^0$ [15].

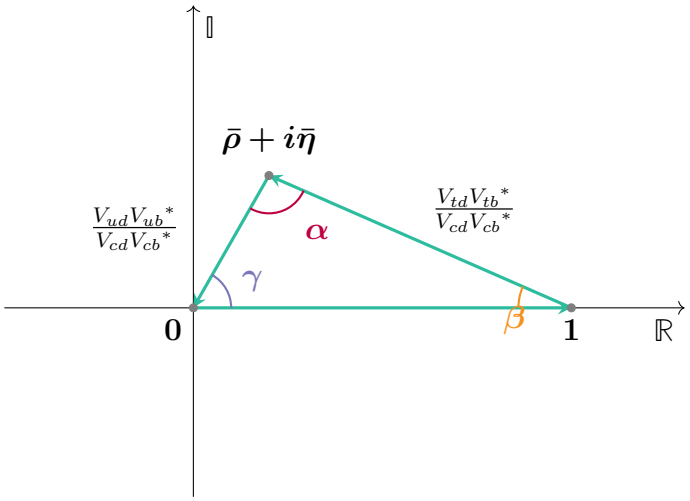

(a) The unitarity triangle given by Eq. (1.10).

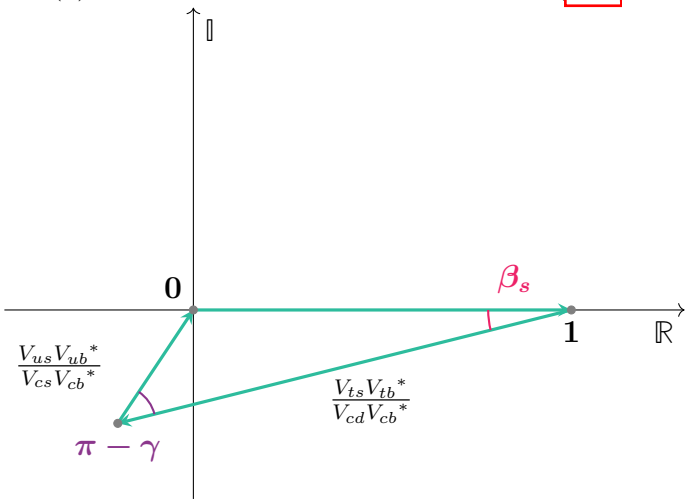

(b) Triangle given by Eq. (1.9).

Figure 1.3: Two unitarity triangles. In the second one, the d quarks are replaced by s ones.

1.3 $\mathcal{CP}$ violations

1.3.1 Discrete symmetries

In physics, a system is said to be *symmetric* if some of its properties are preserved under certain transformations. Continuous symmetries are described by continuous Lie groups and, according to Noether's theorem [17], are linked to conserved continuous quantities (charges and their corresponding currents); discrete symmetries, on the other hand, follow the mathematical formalism of discrete groups and account for discrete conserved quantities.

In particle physics, there are three important discrete symmetries: charge conjugation $\mathcal{C}$, space parity[6] $\mathcal{P}$ and time reversal $\mathcal{T}$. We can define the corresponding transformations and describe them with a self-adjoint operator that acts on a generic state $|\psi(\boldsymbol{x}, \boldsymbol{Q}, t)\rangle$, by inverting

[6] Or simply "parity".

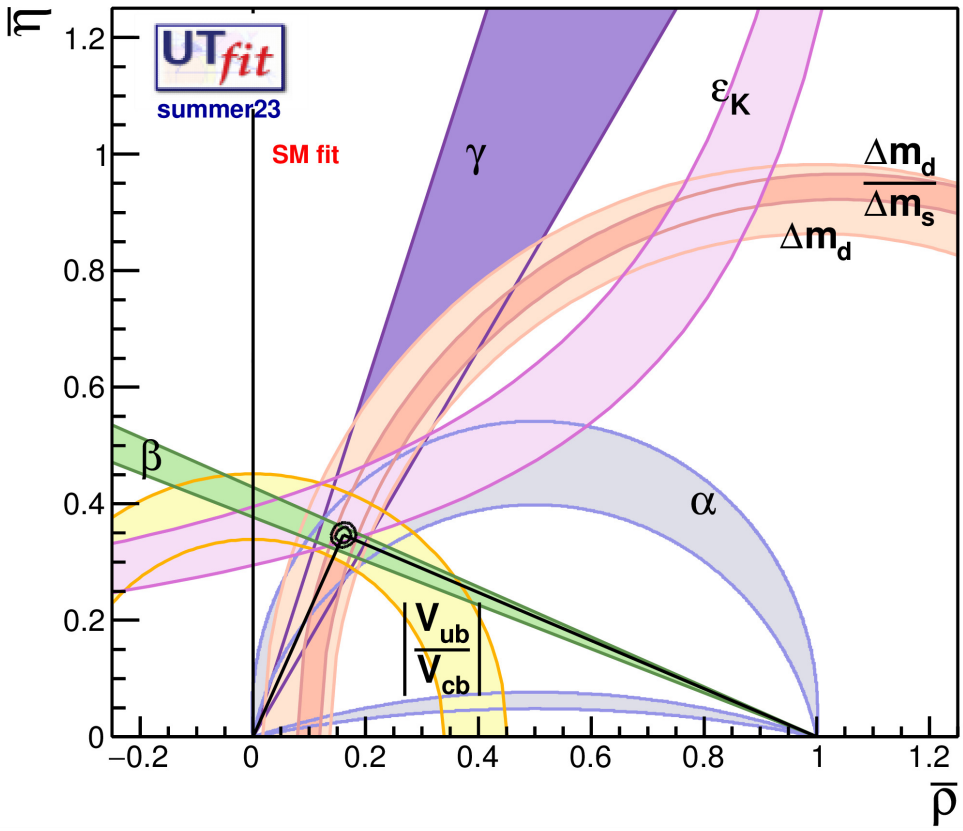

Figure 1.4: Unitarity triangle with constraints of various parameters, as of 2023, performed by the UT*fit* collaboration [15].

the position $\boldsymbol{x}$, the vector of internal charges $\boldsymbol{Q}$ or time t:

$$\begin{cases} \mathcal{C}\ |\psi(\boldsymbol{x},\boldsymbol{Q},t)\rangle = |\psi(\boldsymbol{x},-\boldsymbol{Q},t)\rangle \\ \mathcal{P}\ |\psi(\boldsymbol{x},\boldsymbol{Q},t)\rangle = |\psi(-\boldsymbol{x},\boldsymbol{Q},t)\rangle \\ \mathcal{T}\ |\psi(\boldsymbol{x},\boldsymbol{Q},t)\rangle = |\psi(\boldsymbol{x},\boldsymbol{Q},-t)\rangle. \end{cases}$$

For any of the three discrete operators, which we generically denote with $\mathcal{D}$, we can notice that

$$\mathcal{D}^2\ |\psi\rangle = \mathbb{1}\ |\psi\rangle = \lambda\,\mathcal{D}\ |\psi\rangle = \lambda^2\ |\psi\rangle$$

and thus the eigenvalues are $\lambda = \pm 1$. A state is said to have defined space parity (or charge parity) if it is an eigenstate of $\mathcal{P}$ (or $\mathcal{C}$).

An important theoretical result is the $\mathcal{CPT}$ theorem, that states that every Lorentz-invariant local field theory with a Hermitian Hamiltonian is symmetric under a $\mathcal{CPT}$ transformation (i. e. all three operators are applied, in any order) [18]. As $\mathcal{CPT}$ symmetry implies the equality of masses of a particle and its antiparticle, observable quantities which could falsify the theorem are, for instance, the difference in mass of e^+/e^- or of $K^0/\overline{K}^0$; the values as of

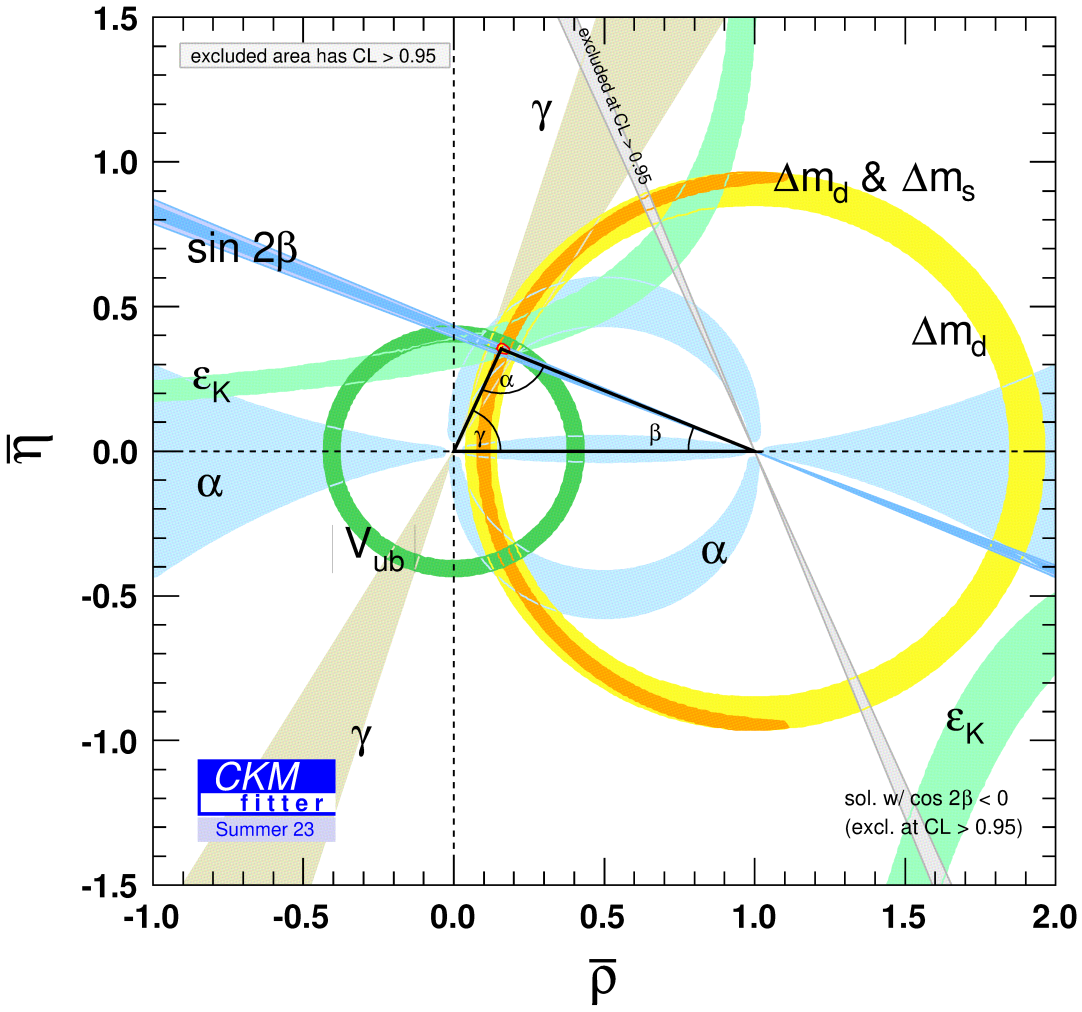

Figure 1.5: Unitarity triangle with constraints of various parameters, as of 2023, performed by the CKMfitter collaboration [16].

April 2024 are compatible with the theorem:

$$2\,\frac{|m_{K^0} - m_{\overline{K}^0}|}{m_{K^0} + m_{\overline{K}^0}} < 6 \times 10^{-9}$$
$$2\,\frac{|m_{e^+} - m_{e^-}|}{m_{e^+} + m_{e^-}} < 8 \times 10^{-9}$$

at 90% CL [13].

1.3.2 $\mathcal{CP}$-violating mechanisms

Up until the first half of the XX century, it was a common belief that all physical laws were invariant to the application of any of the three aforementioned discrete operators. This was proven wrong in 1956, when Wu et al. performed a famous experiment that highlighted that neither $\mathcal{C}$ nor $\mathcal{P}$ are conserved in ^{60}Co β^- decay [19]. A few years later, in 1964, Cronin, Fitch et al. observed the $K_L^0 \to \pi\pi$ decay, a process that violated $\mathcal{CP}$ symmetry [20]. This result, as well as the subsequent experiments that confirmed it, shocked the scientific community: in order to preserve $\mathcal{CPT}$ symmetry, a $\mathcal{CP}$ violation implies a $\mathcal{T}$ violation. In other words, some subatomic-scale processes occur differently depending on the flow of time, something that was thought to be true only for macroscopic systems.

$\mathcal{CP}$ can be violated in three different ways:

1. **Direct** violation, if a particle and its antiparticle have different decay rates,
2. **Indirect** (or **mixing**) violation, if the probability for a particle to oscillate and become its antiparticle is different from the opposite process,
3. **Interference** of direct and indirect violation.

1.3.2.1 Direct $\mathcal{CP}$ violation

Consider a generic decay process $X \to Y$ and its corresponding anti-process $\overline{X} \to \overline{Y}$, where $\overline{X}$ and $\overline{Y}$ are the antiparticles of X and Y. The process is said to directly violate $\mathcal{CP}$ if

$$|A|^2 \equiv |\Gamma(X \to Y)| \neq |\Gamma(\overline{X} \to \overline{Y})| \equiv |\overline{A}|^2,$$

where Γ is the decay width of the process. We can define an observable quantity related to $\mathcal{CP}$ violation:

$$\mathcal{A}_{\mathcal{CP}} \equiv \frac{\Gamma(X \to Y) - \Gamma(\overline{X} \to \overline{Y})}{\Gamma(X \to Y) + \Gamma(\overline{X} \to \overline{Y})} = \frac{|A|^2 - |\overline{A}|^2}{|A|^2 + |\overline{A}|^2} = \frac{1 - \left|\frac{\overline{A}}{A}\right|^2}{1 + \left|\frac{\overline{A}}{A}\right|^2}.$$

It is important to notice that direct $\mathcal{CP}$ violation cannot occur if $|A| = |\overline{A}|$.

An example of a directly $\mathcal{CP}$-violating process is the $B^0 \to \pi^- K^+$ decay and its $\mathcal{CP}$-conjugate $\overline{B}^0 \to \pi^+ K^-$, for which

$$\mathcal{A}_{\mathcal{CP}} = -0.0824 \pm 0.0033 \pm 0.0033,$$

where the first uncertainty is statistical and the second is systematic [21].

1.3.2.2 Meson oscillation and indirect $\mathcal{CP}$ violation

Neutral mesons are allowed to oscillate (see Fig. 1.6) between two $\mathcal{CP}$-conjugated states (i. e. particle and antiparticle) $|M\rangle$ and $|\overline{M}\rangle$, which compose the flavour basis. In fact, their mass eigenstates $|M_1\rangle$ and $|M_2\rangle$ are in a superposition of states of the flavour basis:

$$|M_1\rangle = p\,|M\rangle + q\,|\overline{M}\rangle$$
$$|M_2\rangle = p\,|M\rangle - q\,|\overline{M}\rangle$$

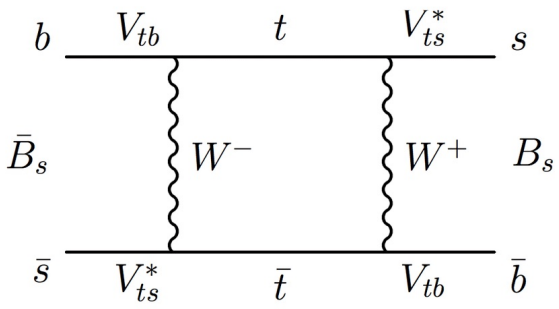

Figure 1.6: Diagram of B_s^0 mixing [22].

where $p, q \in \mathbb{C}$ and $|p|^2 + |q|^2 = 1$.

In this case, the $\mathcal{CP}$-violation observable is defined as:

$$\mathcal{A}_{CP}(M;t) \equiv \frac{\Gamma(\overline{M} \to M;t) - \Gamma(M \to \overline{M};t)}{\Gamma(\overline{M} \to M;t) + \Gamma(M \to \overline{M};t)}, \tag{1.12}$$

where Γ is the probability of the oscillation.

The mass eigenstates depend on time exponentially; in the flavour basis, this is expressed by:

$$\begin{pmatrix} |M(t)\rangle \\ |\overline{M}(t)\rangle \end{pmatrix} = Q \begin{pmatrix} e^{-(im_1+\Gamma_1/2)t} & 0 \\ 0 & e^{-(im_2+\Gamma_2/2)t} \end{pmatrix} Q^{-1} \begin{pmatrix} |M\rangle \\ |\overline{M}\rangle \end{pmatrix},$$

where $m_{1,2}$ and $\Gamma_{1,2}$ are the masses and decay widths of the two mass eigenstates, and

$$Q = \begin{pmatrix} p & p \\ q & -q \end{pmatrix}. \tag{1.13}$$

We can rewrite, for convenience,

$$Q \begin{pmatrix} e^{-i(im_1+\Gamma_1/2)t} & 0 \\ 0 & e^{-i(im_2+\Gamma_2/2)t} \end{pmatrix} Q^{-1} = \begin{pmatrix} g_+(t) & \frac{q}{p} g_-(t) \\ \frac{p}{q} g_-(t) & g_+(t) \end{pmatrix}$$

so that Eq. (1.13) yields

$$|M(t)\rangle = g_+(t)\,|M\rangle + \frac{q}{p} g_-(t)\,|\overline{M}\rangle, \tag{1.14}$$

$$|\overline{M}(t)\rangle = \frac{p}{q} g_-(t)\,|M\rangle + g_+(t)\,|\overline{M}\rangle. \tag{1.15}$$

Two parameters often found in literature are

$$x \equiv \frac{\Delta m}{\Gamma} \qquad y \equiv \frac{\Delta\Gamma}{2\Gamma},$$

where $\Delta m = |m_2 - m_1|$, $\Delta\Gamma = |\Gamma_2 - \Gamma_1|$ and $\Gamma = \frac{\Gamma_1+\Gamma_2}{2}$. These parameters are useful, as we can write

$$|g_\pm(t)|^2 = \frac{e^{-\Gamma t}}{2}\left[\cosh\left(\frac{\Delta\Gamma}{2}t\right) \pm \cos(\Delta m t)\right] = \frac{e^{-\Gamma t}}{2}\left[\cosh\left(y\,\Gamma\,t\right) \pm \cos(x\,\Gamma\,t)\right].$$

Using

$$\Gamma(X \to Y, t) = |\langle Y|X(t)\rangle|^2$$

and Eqs. (1.14), (1.15) we get some useful expressions for the oscillation probabilities:

$$\Gamma(M \to M, t) = \Gamma(\overline{M} \to \overline{M}, t) = |g_+(t)|^2, \tag{1.16}$$

$$\Gamma(M \to \overline{M}, t) = \left|\frac{q}{p}\right|^2 |g_-(t)|^2, \tag{1.17}$$

$$\Gamma(\overline{M} \to M, t) = \left|\frac{p}{q}\right|^2 |g_-(t)|^2, \tag{1.18}$$

where we used the properties of orthonormalization of the flavour basis: $\langle M|M\rangle = \langle\overline{M}|\overline{M}\rangle = 1$ and $\langle M|\overline{M}\rangle = 0$.

Substituting Eq. (1.16), (1.17) and (1.18) into Eq. (1.12) we get

$$\mathcal{A}_{\mathcal{CP}} = \frac{\left|\frac{q}{p}\right|^2 |g_-(t)|^2 - \left|\frac{p}{q}\right|^2 |g_-(t)|^2}{\left|\frac{q}{p}\right|^2 |g_-(t)|^2 + \left|\frac{p}{q}\right|^2 |g_-(t)|^2} = \frac{1 - \left|\frac{p}{q}\right|^4}{1 + \left|\frac{p}{q}\right|^4},$$

an expression that highlights how indirect $\mathcal{CP}$ violation only happens when $|p/q| \neq 1$.

Examples of indirectly $\mathcal{CP}$-violating processes are the already mentioned $K_L \to \pi\pi$ and $K \to \pi\ell\nu$ [13].

1.3.2.3 Interference between direct and indirect $\mathcal{CP}$ violation

In some processes, both X and its $\mathcal{CP}$-conjugate $\overline{X}$ can decay in the same state f. This means that the direct decay $X \to f$ and the mixed one $X \to \overline{X} \to f$ interfere.

Here, we define

$$\mathcal{A}_{\mathcal{CP}}(t) = \frac{\Gamma(\overline{X} \to f; t) - \Gamma(X \to f; t)}{\Gamma(\overline{X} \to f; t) + \Gamma(X \to f; t)} \tag{1.19}$$

It can be shown that, if we consider indirect $\mathcal{CP}$ violation negligible compared to the direct one (i. e. $|p/q| \approx 1$), Eq. (1.19) can be rewritten as

$$\mathcal{A}_{\mathcal{CP}}(t) = \frac{-C_f \cos(\Delta m\, t) + S_f \sin(\Delta m\, t)}{\cosh\left(\frac{\Delta\Gamma}{2}t\right) + D_f \sinh\left(\frac{\Delta\Gamma}{2}t\right)} \tag{1.20}$$

where

$$C_f = \frac{1 - |\lambda_f|^2}{1 + |\lambda_f|^2}, \quad D_f = \frac{2\,\mathrm{Re}\{\lambda_f\}}{1 + |\lambda_f|^2}, \quad S_f = \frac{2\,\mathrm{Im}\{\lambda_f\}}{1 + |\lambda_f|^2} \tag{1.21}$$

and

$$\lambda_f = \frac{q}{p}\frac{\overline{A}}{A}.$$

1.3.3 B^0 and B_s^0 mesons

B mesons are hadrons composed of a beauty antiquark and an up (B^+ meson), charm (B_c^+), down (B^0) or strange (B_s^0) quark. The B^0 and B_s^0 are of particular interest as they are neutral and thus oscillate with their antiparticle, as discussed in Sec. 1.3.2.2. In addition to that, the b quark, being the heaviest quark to form bound states ($m_b = 4.18^{+0.03}_{-0.02}\,\mathrm{GeV}/c^2$ [13]), decays in many different ways, giving the opportunity to observe rare processes and $\mathcal{CP}$ violation. The current values of $\mathcal{CP}$-violating parameters of some B^0 and B_s^0 decays, which, in this case, are given by the interference of direct and indirect violation (see Sec. 1.3.2.3), are presented in Tab. 1.1.

Process	$\boldsymbol{C_f}$	$\boldsymbol{S_f}$
$B^0 \to \pi^+\pi^-$	-0.31 ± 0.03	-0.67 ± 0.03
$B_s^0 \to K^+K^-$	0.16 ± 0.04	0.14 ± 0.05

Table 1.1: $\mathcal{CP}$ violation parameters as of 2025 [13].

Chapter 2

The LHCb Experiment

2.1 Overview

The LHCb experiment is one of the four large detectors at the Large Hadron Collider (LHC). Its primary purpose is to study $\mathcal{CP}$ violation by analysing heavy-flavour hadron decays.

LHCb has operated during the LHC Run 1 (2010–2012) and Run 2 (2015–2018) data-taking campaigns [23]. Afterwards, the detector underwent a series of major technical upgrades, the so-called LHCb Upgrade I [24], that drastically improved its performance during Run 3 (2022-2026), the current data-taking period.

One of the biggest improvements of the LHCb Upgrade I is the possibility of running at a higher luminosity than before. Instantaneous luminosity is a quantity that measures the ability to produce collisions in a particle accelerator, and can be expressed as

$$\mathcal{L}_{inst} = \frac{\mu}{\sigma} N_{bb} \, f_{LHC}$$

where μ is the visible number of interactions per unit time for a given process, σ its cross-section, N_{bb} is the number of colliding bunches within LHC and $f_{LHC} = 11\,245\,\text{Hz}$ is the LHC revolution frequency. A high luminosity is crucial to collect the large amount of data necessary for precise physics measurements.

After the upgrade, LHCb operates at a nominal instantaneous luminosity $\mathcal{L} \approx 2{\times}10^{33}\,\text{cm}^{-2}\,\text{s}^{-1}$, 5 times greater than during the previous runs, but still an order of magnitude smaller than the LHC design luminosity for proton physics, which is currently exploited by the general purpose detectors (ATLAS and CMS). In order to run at lower luminosity, *luminosity levelling* techniques are employed [25, 26]. The levelling is achieved by offsetting the beams in the transverse direction, thereby reducing the overlap region of the two proton bunches. Using a real-time feedback from the experiment, the offset is progressively reduced and the beams are brought closer to each other. The procedure is schematically illustrated in Fig. 2.1. In addition to a lower value, a constant luminosity is achieved too, which optimizes LHCb tracking performance.

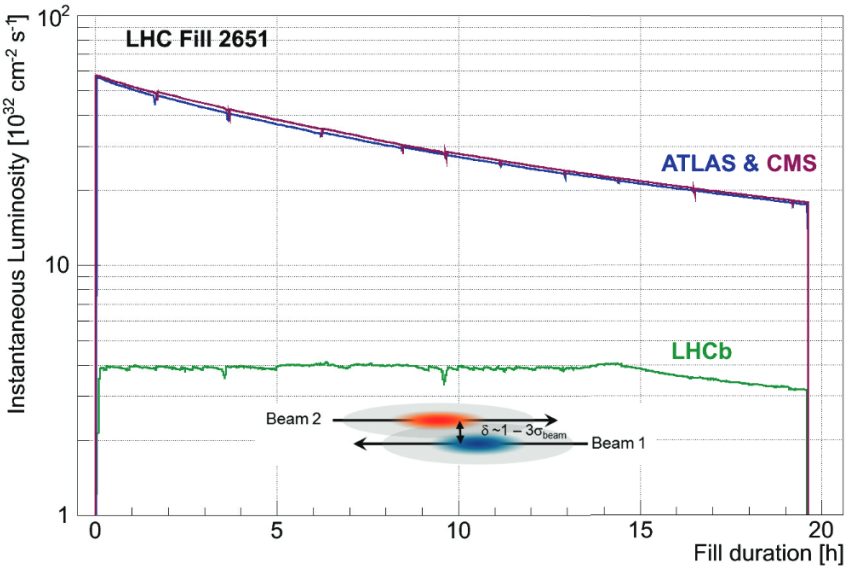

Figure 2.1: Instantaneous luminosity for LHCb, ATLAS and CMS during LHC fill 2651. Note how the former has a stable luminosity (in a range of 5%) for 15 hours. A sketch of the two offset beams is also depicted [27].

2.1.1 Detector components

The Run 3 LHCb detector is a single-arm forward spectrometer covering the pseudorapidity[1] range $2 < \eta < 5$. A right-handed reference frame is defined, as shown in Fig. 2.2, with the z axis parallel to the LHC beam pipe, the y axis pointing upward and perpendicular to the Earth's surface, the x axis pointing to the centre of LHC ring, and the origin in the nominal pp interaction point.

The main components of the LHCb detector are:

- **VELO**, the vertex locator;
- **RICH1** and **RICH2**, two ring imaging Cherenkov detectors;
- **UT**, a silicon-strip upstream tracker;
- the **magnet**;
- **SciFi**, a scintillating-fibre tracker;
- **ECAL** and **HCAL**, an electromagnetic and a hadronic calorimeter;
- **M2-M5**, four[2] muon detectors.

[1] Pseudorapidity is a spacial coordinate widely used in particle physics. It is defined as $\eta = -\ln(\tan(\theta/2))$, where θ is the angle relative to the beam axis.

[2] In the original design there was a fifth muon detector, M1, which has been removed in the upgrade [28].

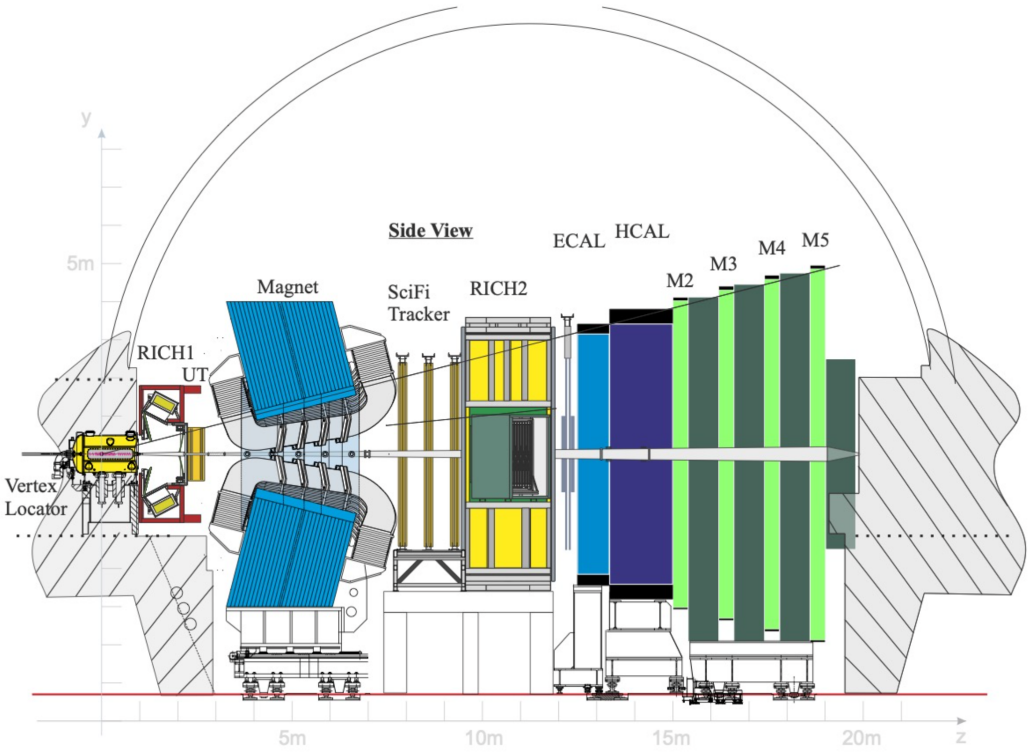

Figure 2.2: Layout of the LHCb detector after Upgrade I [24].

Other auxiliary components are PLUME[3], a dedicated luminometer composed of 48 photomultiplier tubes (PMTs) [29]; two Beam Conditions Monitor systems (BCM), each consisting of eight poly-crystalline chemical vapour deposition diamond pad sensors [30]; a Radiation Monitor System (RMS) made of four metal-foil detector modules [31]; and a gas injection system, SMOG2[4], which infuses He, Ne, or Ar directly into the LHC beam pipe, giving the opportunity to operate LHCb in fixed-target mode too [32]. The two main purposes of the detectors are particle identification (PID) and tracking of their trajectories. In order to achieve these goals, it is crucial to have an effective triggering system.

2.2 Tracking

By *tracking*, we mean the reconstruction of a particle trajectory and the measurement of the sign of its charge and of its kinematic quantities. This task is carried out mainly by the VELO, the UT, the SciFi, and the magnet.

[3]Probe for LUminosity MEasurement.
[4]System for Measuring the Overlap with Gas.

2.2.1 VELO

The vertex locator, as the name suggests, has the objective of locating the positions of primary vertices (PV) of pp interactions, and secondary vertices, i. e. where the produced particles decay. It does this by detecting the hits of ionizing particles, which produce free electrons and electron holes in its silicon detectors.

As a spatial offset results in a temporal error, it is of utmost importance to perform very precise measurements of the vertices' positions in order to carry out time-dependent analyses (see Sec. 3.1 for an estimate of the effects of a time bias).

The VELO is made of 52 L-shaped pixelated hybrid silicon modules (see Fig. 2.3), operating in vacuum conditions and at a temperature of $-20\,^{\circ}\mathrm{C}$ thanks to a bi-phase CO_2 silicon cooling system [33]. See Tab. 2.1 for a list of other VELO parameters.

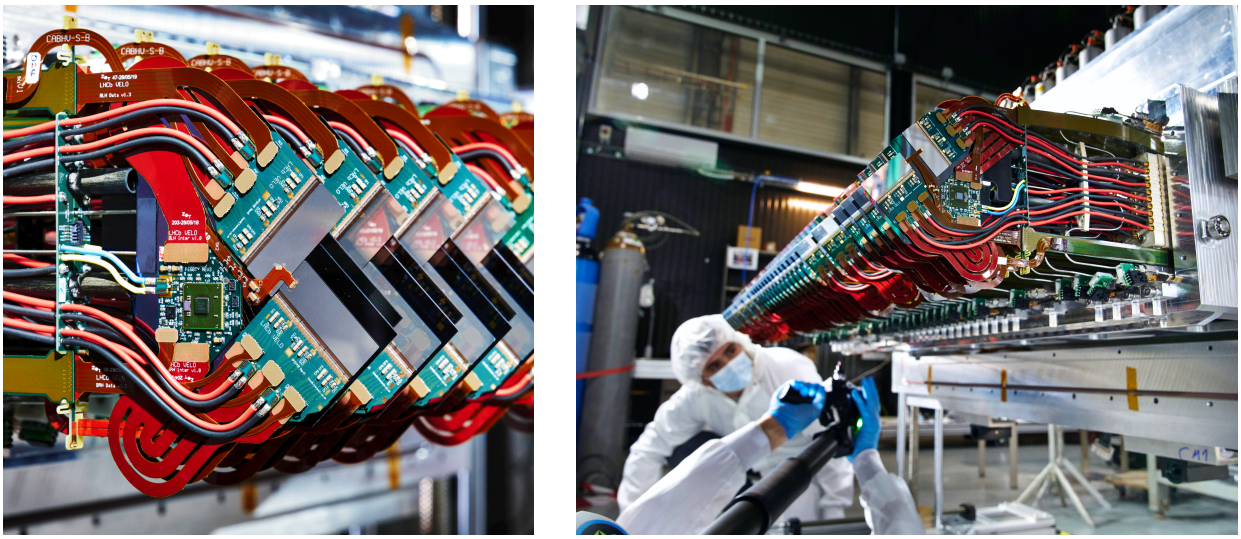

Figure 2.3: On the left, a VELO module; on the right, half of the VELO during the assembly.

The modules are arranged in two rows, parallel to the beam pipe. The row with positive x is referred to as *side C*, the other one as *side A*. The modules are not equispaced, but are instead arranged in a configuration with a higher concentration of modules around the pp interaction point (see Fig. 2.4), so that most tracks from the interaction region traverse at least four sensors, for all azimuthal directions. During the beam collimation phase, the VELO is in the open configuration, i. e. with the two halves far apart, in order to prevent the beam from hitting its modules, as this would damage them. Once the beams are collimated, the VELO is set in the closed configuration, in which the modules come closer and partially overlap, arriving at a distance of $\approx 7\,\mathrm{mm}$ from the beam. In order to overlap, the modules have a relative z offset of 12.5 mm.

The VELO is subject to mechanical drifting, mainly because of the thermal dilation of the metallic structure that holds the silicon modules and its interaction with the residual magnetic field of the LHCb magnet. To try and reduce this effect (that affects the precision of the vertices position measurements), around every 10 minutes some parameters that reflect the precision of the VELO alignment are assessed, and whenever their values indicate a significant

Parameter	pre-upgrade	post-upgrade
RF box inner radius (minimum thickness)	5.5 mm (300 µm)	3.5 mm (150 µm)
Inner radius of active silicon detector [mm]	8.2	5.1
Total fluence (silicon tip) [$n_{\text{eq}}/\text{cm}^2$]	4×10^{14}	$\approx 8 \times 10^{15}$
Sensor segmentation	r–ϕ strips	square pixels
Total active area of Si detectors [m^2]	0.22	0.12
Pitch (strip or pixel) [µm]	37–97	55
Technology	n-on-n	n-on-p
Number of modules	42	52
Total number of channels	170 000	41×10^6
Readout rate [MHz]	1, analogue	40, zero suppressed
Whole-VELO data rate [Gbit/s]	150	≈ 2000
Total power dissipation (in vacuum) [W]	800	≈ 2000

Table 2.1: VELO parameters before and after the upgrade [24].

deviation, alignment constants are updated.

2.2.2 UT

The Upstream Tracker is a silicon-strip detector made of four planar detectors (see Fig. 2.5) organized in two stations (UTa and UTb) [34].

The first and last panel detect the x coordinate of a charged particle that passes through it (and are thus called UTaX and UTbX), while the second and third ones measure the y component through a stereo angle of $\pm 5°$.

As the UT has to cover occupancies and radiation fluences spanning different orders of magnitude [24], different microstrip sensors are used. Those in the central region (yellow and pink in Fig. 2.5) are n-in-p and have a hit resolution of 27 µm, while sensors in the outer part (green in Fig. 2.5) are p-in-n and achieve a hit resolution of 55 µm.

The main utility of the UT is that, by combining its hits with the VELO tracks, a first estimate (with a precision of 15%) of a particle momentum is performed, which speeds up the matching with the SciFi tracker and the whole matching algorithm. In addition to that, the UT allows for the detection of long-lived particles (e.g. K_s^0 and Λ) that decay after the VELO.

2.2.3 Magnet

The LHCb magnet (see Fig. 2.6) consists of two identical, saddle-shaped coils mounted into a window-frame yoke, each made of 15 aluminium mono-layer pancakes, with 15 turns per

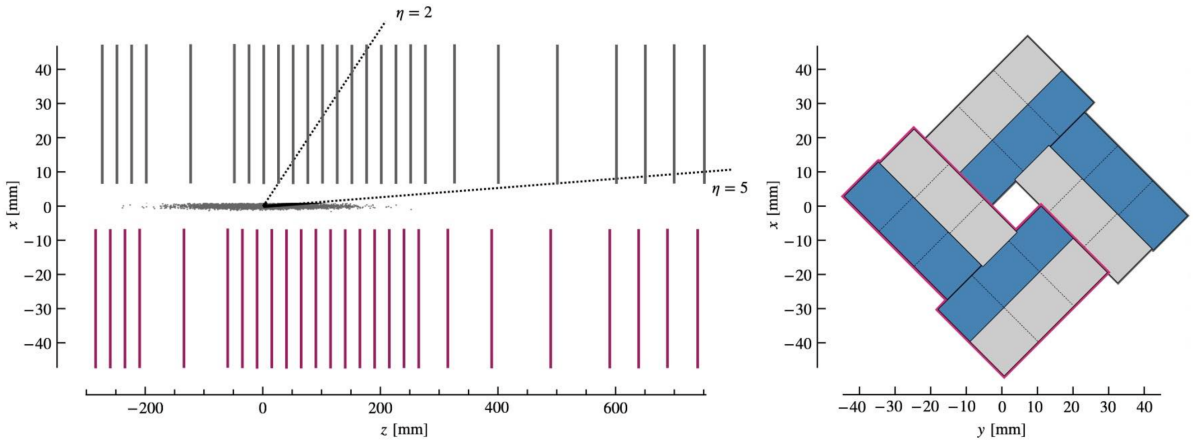

Figure 2.4: On the left: VELO seen from above on the xz plane, at $y = 0$. The luminous region and the nominal LHCb pseudorapidity acceptance are illustrated too. On the right: VELO seen on the xy plane. The modules of the negative x side (side A) are highlighted in purple. Both figures depict the closed configuration [24].

pancake. The current flowing in them is 5.8 kA; the magnet produces a field mainly directed along the z axis with a maximum intensity 1.1 T and an integrated bending power 4 T m [35].

As it is a warm magnet (i. e. not a superconducting one), it is possible to reverse its polarity. This is done frequently during data taking in order to mitigate possible detector-induced asymmetries, namely left-right asymmetries arising from the fact that charged particles bend preferentially to one side of the experiment under the effect of a magnetic field of a given polarity.

2.2.4 SciFi

The SciFi tracker is composed of 12 detection planes, arranged in 3 stations (T1, T2, and T3). Each plane is made of vertical strips (2.4 m long and 13 cm wide); the strips are composed of many layers of plastic scintillating fibres [24].

Similarly to the UT (see Sec. 2.2.2), in each of the three stations the first and last planes detect the x coordinate of the particle hit, while the second and third have their strips rotated by $\pm 5°$ with respect to the y axis, in order to measure the y coordinate of the track. The mean hit efficiency (excluding gaps) is estimated to be $(99.3 \pm 0.2)\%$, while the single hit resolution (for perpendicular tracks) is (64 ± 16) µm [24].

2.3 Particle identification

Particle identification (PID) is the determination of what kind of particle was detected. This is achieved by combining the information coming from RICH1 and RICH2, the two calorimeters, and the muon detectors.

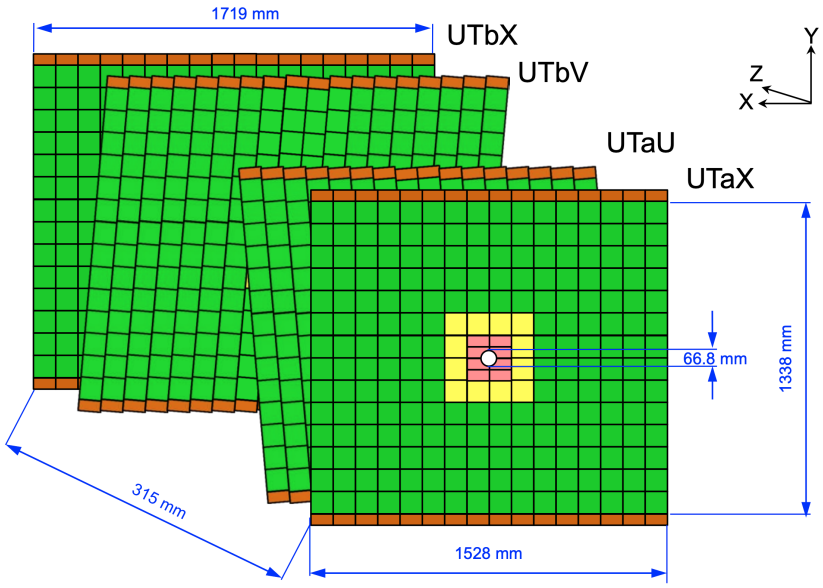

Figure 2.5: The four UT planes, divided into the two stations. Each box is a sensor; different colours represent different sensor types [34].

2.3.1 RICHs

The Cherenkov effect is the emission of photons that occurs when an electrically charged particle moves through a medium with a speed v_p faster than the speed of light in that medium. The photons are emitted at an angle θ_C with respect to the particle direction, with

$$\cos\theta_C = \frac{1}{n\beta} + \frac{\sqrt{1-\beta^2}}{\beta}\frac{\lambda_0}{\lambda} \approx \frac{1}{n\beta},$$

where n is the medium refractive index, $\beta = v_p/c$, λ is the wavelength of light in the medium and λ_0 is the Compton wavelength. The second term, which arises when quantum effects are taken into account, can be neglected in almost any practical case [38].

The two RICHs provide discrimination information for charged particle states. Thanks to their PID capabilities of hadronic final states, it is possible to discriminate otherwise identical topologies as $B^0 \to \pi^+\pi^-, K^+\pi^-, K^+K^-$; in addition to that, they reduce the combinatorial background in decays with hadrons in their final state, and contribute to determining the flavour of a $B^0_{(s)}$ at production [24].

The main components of each of the two RICHs (see Fig. 2.8a) are a fluorocarbon gas radiator, a system of spherical and planar mirrors that reflect and focus the Cherenkov photons, and multi-anode photomultiplier tubes to detect them. Once the photons are detected, an algorithm [39] determines the most likely mass of a particle for that signal. In a nutshell, this works as follows: after a pattern recognition (due to the mirrors, the photons that arrive on detector planes create a circular shape, see Fig. 2.8b), the likelihood of a default π hypothesis is computed; then, different mass hypotheses are tested until the likelihood is maximised.

RICH1 uses a C_4F_{10} gas radiator ($n = 1.0014$) and is located upstream of the magnet, providing PID in the momentum range between 2.6 and 60 GeV/c. RICH2, on the other hand,

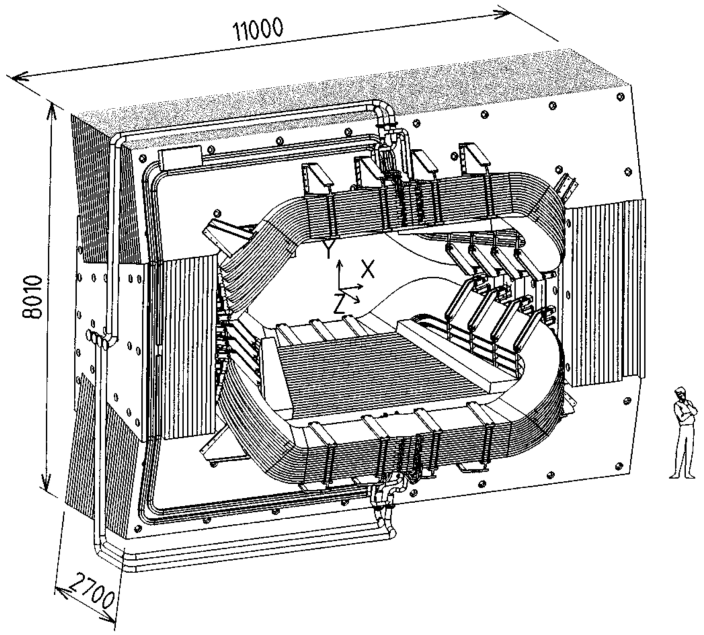

Figure 2.6: LHCb's magnet (lengths are in mm) [36].

specializes in detecting particles with higher momentum, between 15 and 100 GeV/c, and is equipped with a CF_4 radiator ($n = 1.0005$) [24]. As n is highly sensitive to temperature and pressure variations, a calibration is performed before each fill [24].

2.3.2 ECAL and HCAL

The two calorimeters are composed of a succession of alternating planes of absorbing and scintillating material divided into cells. Particles that enter the calorimeter interact with the absorbing planes and produce a shower of secondary particles, causing the scintillating material to produce photons that are detected by PMTs. By measuring the energy that is dissipated in the calorimeter, the energy of the primary particles can be calculated.

The ECAL is made of independent Shashlik modules [41]; each module is composed of 4-mm thick scintillating plates and 2-mm thick lead plates perpendicular to the beamline. This calorimeter is specialized in detecting photons and electrons. It is important that these particles are detected with high energy resolution, which requires the full containment of the secondary particles [24]; thus, the thickness of the ECAL is 25 radiation lengths [42]. The relative energy resolution of the ECAL, measured with a test electron beam, is

$$\frac{\sigma(E)}{E} = \frac{(9.0 \pm 0.5)\%}{\sqrt{E}} \oplus (0.8 \pm 0.2)\,\% \oplus \frac{0.3\%}{E \sin\theta} \tag{2.1}$$

where $\oplus$ indicates a quadrature sum, E is the particle energy (in GeV), and θ is the angle between the beamline and the segment that goes from the nominal LHCb interaction point to the ECAL cell. The second term of Eq. (2.1) is relative to the noise of the electronics [24], the third one takes into account miscalibrations, nonlinearities, energy leakage out of the cell, and other effects.

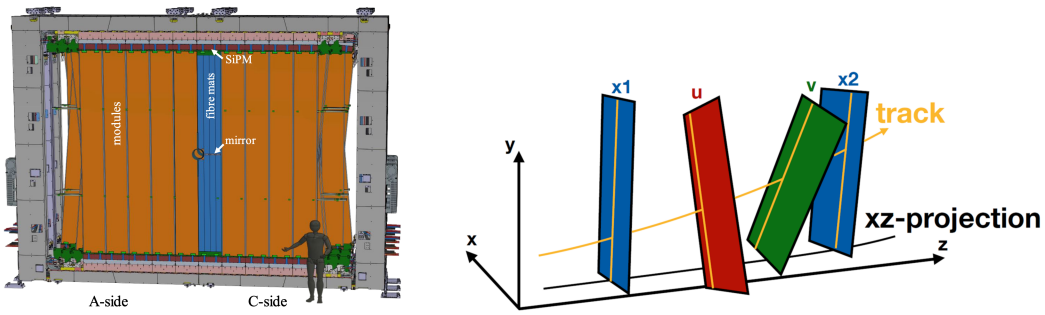

(a) (b)

Figure 2.7: Left: front and side view of the SciFi [24]; right: position of SciFi layers in each station and track of a particle [37].

The HCAL is composed of iron instead of lead, and its planes, unlike the ECAL, are parallel to the beamline. As the trigger conditions do not require an energy resolution as precise as for the ECAL, the HCAL is only 5.6 interaction lengths thick [43]. Its relative energy resolution, measured with a test pion beam, is

$$\frac{\sigma(E)}{E} = \frac{(67 \pm 5)\%}{\sqrt{E}} \oplus (9 \pm 2)\,\%,$$

less precise if compared with Eq. (2.1), as discussed previously.

As shown in Fig. 2.9, the cell subdivision has a higher granularity near the beam pipe, where more particles are produced.

2.3.3 Muon system

The LHCb muon system has the goal of identifying muons; this is a crucial task, as these particles are present in the final states of many $\mathcal{CP}$-sensitive B decays (such as $B^0 \to (J/\psi \to \mu^+\mu^-)K^s_0$ and $B^0_s \to (J/\psi \to \mu^+\mu^-)\phi$) [44]. Moreover, muons are produced in other interesting decays, as the rare $B^0_s \to \mu^+\mu^-$, that could reveal BSM physics, or the $J/\psi \to \mu^+\mu^-$, which is the subject of this thesis.

The muon system is composed of four stations (M2 to M5), with a total of 1104 Multi-Wire Proportional Chambers (MWPC) for a total surface of 385 m^2 [24]. The stations are interleaved with 80-cm thick iron plates that absorb particles with lower penetrating power than muons. As muons can travel through matter for long distances with minimal interactions, the muon system is the component located furthest from the interaction point.

Each MWPC is composed of four 5-mm thick gaps containing a mixture of Ar, CO_2 and CF_4 ($40\% - 50\% - 10\%$) and an array of wires at a positive voltage with respect to the chamber walls (the operating voltage is about 3 kV) [44]. As a muon passes through the MWPC, it creates ion pairs in the gas, which are accelerated by the electric field. Free electrons will ionize other gas particles (a process called Townsend discharge [45]), producing measurable current (the primary ionization is about 100 e^-/cm, the gas gain 10^5) [44].

The four stations are divided into four regions (R1-R4) of increasing size moving further from the beamline, segmented into rectangular *logical pads* (see Fig. 2.10). The granularity

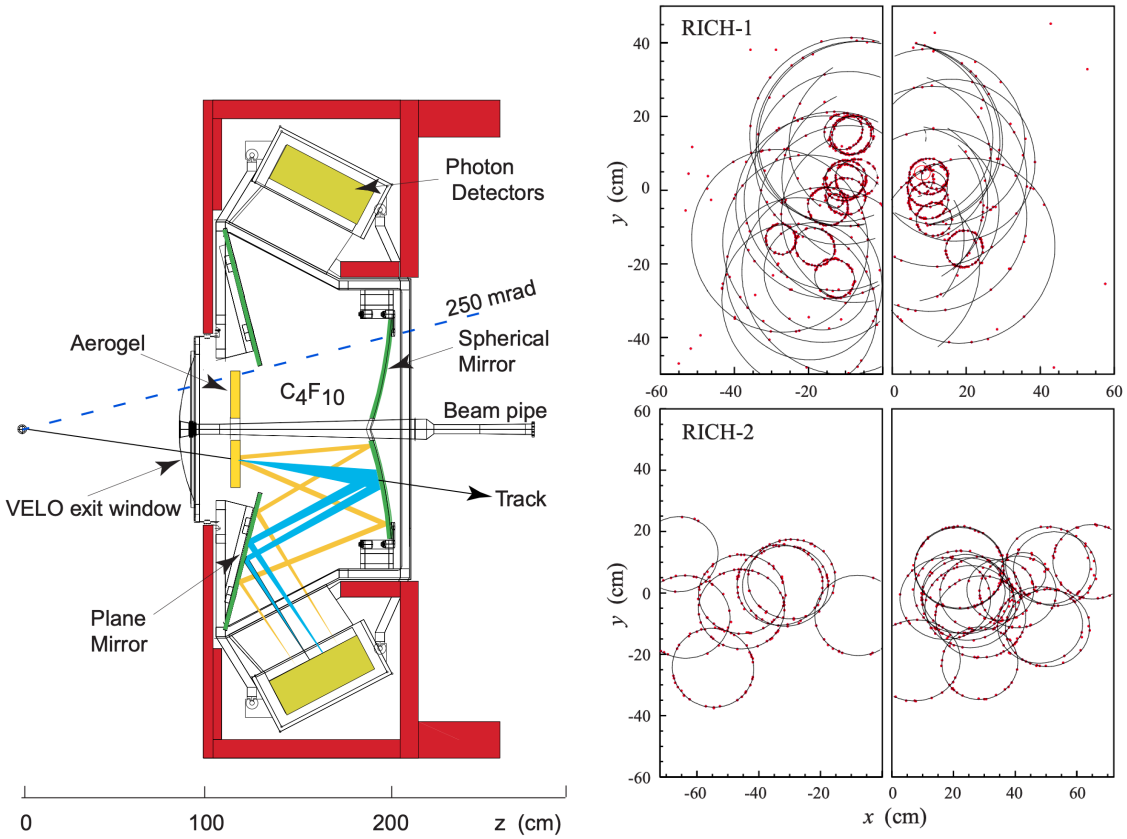

(a) Side view of RICH1. The aerogel has been removed in the upgrade [40].

(b) Detected photons (dots) and circles reconstructed by the algorithm [39].

Figure 2.8: Scheme and functioning of the RICH.

of logical pads increases with the distance from the beamline, as this region is reached by a smaller number of muons; in addition to that, the effect of Coulomb scattering on them is more intense, making a high hit resolution useless.

2.4 Triggering

Triggering is the discarding of uninteresting events in order to work with a more manageable volume of data. At LHCb, one must reduce the $4\,\mathrm{TB\,s^{-1}}$ bandwidth produced by pp collisions at nominal luminosity to the 10 GB/s that can be saved on the permanent offline storage. This is achieved with an all-software trigger that reconstructs events in real time.

The trigger is divided into two stages. The first one, High Level Trigger 1 (HLT1), is an inclusive trigger that reduces the data volume by a factor of 20 and is based primarily on charged particle recognition. The second stage, HLT2, on the other hand, performs quality reconstruction and physical signature selection. Between the two levels, there is a disk buffer with a capacity of about 30 PB (which is equivalent to around 80 hours of data taking).

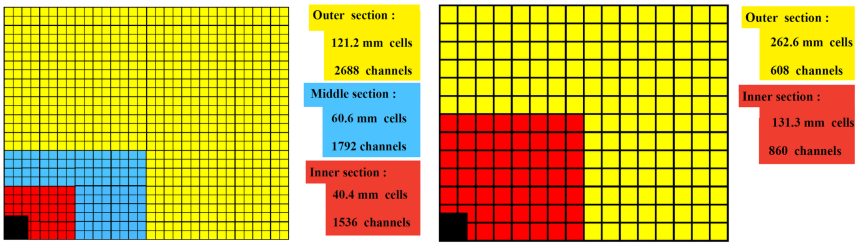

Figure 2.9: ECAL (left) and HCAL (right) cell segmentation [41].

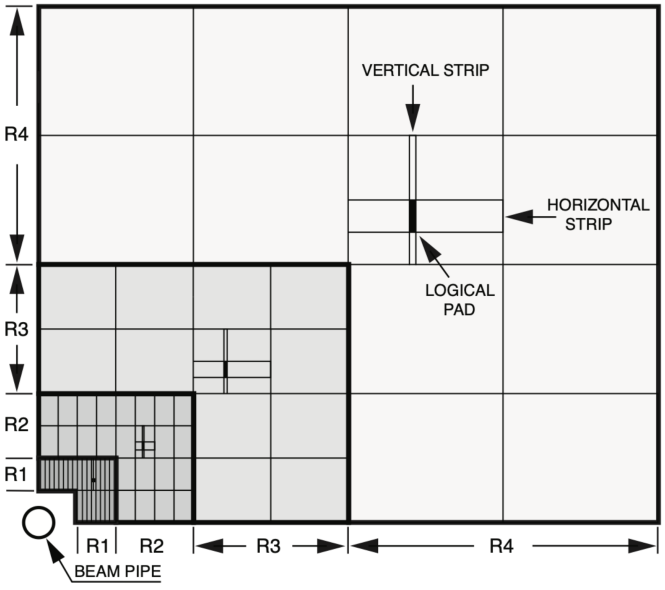

Figure 2.10: Frontal view of one of the quadrants of M2 [44].

2.4.1 HLT1

The HLT1 stage focuses on reconstructing vertices and tracks, and identifying muons. It employs the Allen project, an implementation of $\mathcal{O}(100)$ selection algorithms that run on 600 NVIDIA RTX A5000 GPUs[5]. Allen is the first complete high-throughput GPU trigger used in a high-energy physics experiment [46].

In summary, the sequence of HLT1 is:

1. a Global Event Cut (GEC) is performed: 10% of events (based on UT and SciFi data) with the higher number of tracks are rejected, as they have a high computational time cost and a lower reconstruction efficiency;

2. tracks and PVs are reconstructed in the VELO;

3. tracks are extrapolated to the UT and, subsequently, to the SciFi, but only if above a transverse momentum[6] threshold (in the baseline configuration, the limit is 500 MeV/c);

4. using parametrized Kalman filtering [47], the position of the particle in the beam line is estimated. Then, the particle displacement from primary vertices is calculated;

5. tracks are identified as muons or non-muons, and combined to form two-body vertices.

Various selections are applied to the features of the events that are determined with this sequence. The selection triggers can be divided into four categories [24]:

1. a primary inclusive selection, for the majority of direct physics data taking;

2. selections for specific physics signatures not covered by the first trigger;

3. selections for calibration samples (to perform data-driven evaluations of the reconstruction performance);

4. technical triggers (for luminosity determination, monitoring, calibration and alignment).

Some of the primary inclusive selections are:

- a *displaced single track* and a *two track vertex trigger*, which require large transverse momentum and significant displacement from all PVs. This selects only particles that are produced boosted along the z axis and have a non-negligible lifetime, as B^0 and B_s^0 mesons;

- a *displaced single μ trigger* and *displaced double μ trigger*, which are similar to the previous triggers, but requires the track(s) to be of a muon, and relaxes the p_T and displacement requirements;

[5] GPUs are particularly convenient to use as many HLT1 tasks lend themselves to a very high degree of parallelization.

[6] Transverse momentum, often indicated with p_T, is the magnitude of the projection of the particle momentum on the plane perpendicular to the beamline.

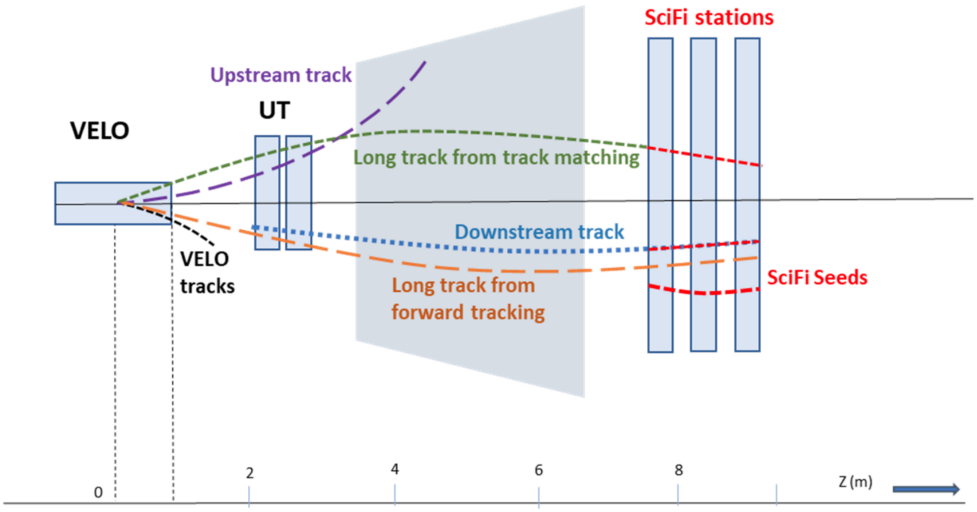

Figure 2.11: Different track types. Long tracks have the most precise momentum determination, and are used in almost all LHCb analyses [24], as the one in Chapter 3 of this thesis.

- a *high-mass double μ trigger*, which requires the invariant mass of the two μ to be above 2900 MeV/c, and does not make any p_T or displacement filtering. This is important to detect decays such as $J/\psi \to \mu^+\mu^-$;

- a *very high transverse momentum muon trigger*, which bypasses the GEC, and is used for electroweak physics and searches for exotic signatures.

2.4.2 HLT2

The HLT2 stage performs offline quality reconstruction and, using $\mathcal{O}(1000)$ algorithms, applies selection filters to determine which events are retained and how much of their information to store.

It is implemented in the Moore project and runs on server CPUs in the Event Filter Farm of LHCb data centre, in an asynchronous way (i. e. not necessarily immediately after HLT1).

The reconstruction is divided into four parts:

- *charged particles recognition*: various tracking algorithms reconstruct the traces of the particles, which can be of different types, as shown in Fig. 2.11. This is done by combining data from the VELO, UT and SciFi and by taking into account the magnet's effect. An example of tracking algorithm can be found at [37];

- *Kalman filter*: using parametric or non-parametric Kalman filters, the properties of the trajectories of charged particles are calculated with precision;

- *calorimeter reconstruction*: multivariate algorithms based on secondary particles showers shapes are used to measure the energy of particles hitting the calorimeters;

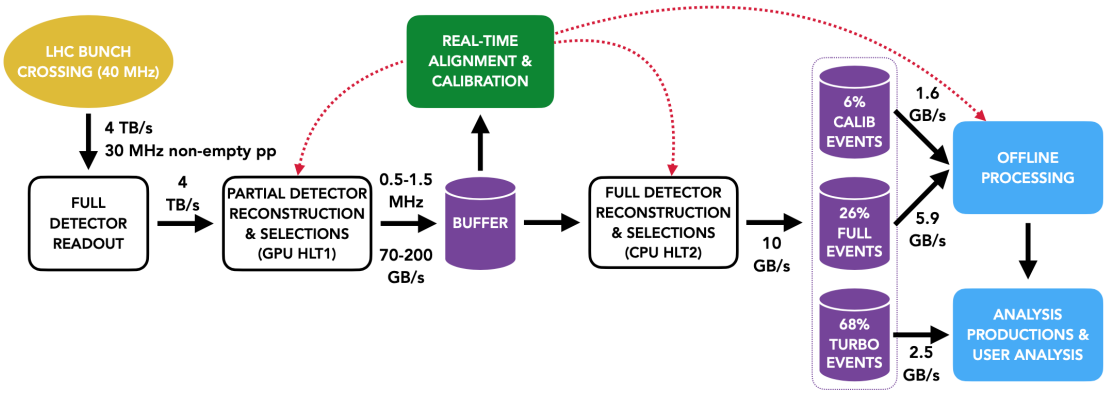

Figure 2.12: The LHCb data flow [50].

- *particle identification*: dedicated algorithms use data from the two RICHs, the ECAL and the muon system to identify five long lived particles: electrons, muons, pions, kaons and protons. Other particles are identified by non-centralized algorithms.

Unlike HLT1, where a few selections could comprehend almost all interesting events, HLT2 uses around 1000 different filters [24], each tailored for a specific topology or physical analysis. Once an event has been selected, the amount of information to be kept is decided, varying from the small Turbo events, which save only tracks and vertex coordinates, up to the Full events, which store all the available information [48, 49]. The full data flow, from the trigger to the offline data storage, is shown in Fig. 2.12.

Chapter 3

Data Analysis

In this section, the data-driven analysis on prompt $J/\psi \to \mu^+\mu^-$ to determine the decay-time bias and resolution is presented. First, an invariant-mass fit has been performed in order to subtract the combinatorial background. Then, after dividing the sample into different bins over seven different kinematic variables, a decay-time fit has been carried out. As it will be shown shortly, the bias and resolution can be computed from the mean and standard deviation of the Gaussian function modelling the decay-time signal.

3.1 Bias and resolution effects on $\mathcal{A}_{\mathcal{CP}}(t)$

As seen in Sec. 1.3.2.3, the time-dependent $\mathcal{CP}$ asymmetry due to $\mathcal{CP}$ violation in the interference between mixing and decay can be written as

$$\mathcal{A}_{\mathcal{CP}}(t) = \frac{-C_f \cos(\Delta m\, t) + S_f \sin(\Delta m\, t)}{\cosh\left(\frac{\Delta\Gamma}{2}t\right) + D_f \sinh\left(\frac{\Delta\Gamma}{2}t\right)} \tag{3.1}$$

This equation tells us the importance of having maximal precision in decay time measurements. We consider, as an example, the B_s^0 meson, for which $\Delta m = (17.741 \pm 0.020) \times 10^{12}\,\hbar/\mathrm{s}$ [15], and, for the $B_s^0 \to K^+K^-$ process, $S_f = 0.123 \pm 0.034 \pm 0.015$ and $C_f = 0.164 \pm 0.034 \pm 0.014$ [21].

Suppose that the measurement of the decay time has a negative bias of magnitude $\delta = 3 \times 10^{-15}\,\mathrm{s}$, an error three orders of magnitude smaller than the B_s^0 mean life $\tau = (1.520 \pm 0.005) \times 10^{-12}\,\mathrm{s}$ [13].

If we consider the approximation of Eq. (3.1) for $\frac{\Delta\Gamma}{2}\, t \ll 1$, reasonably good since $\Delta\Gamma_{B_s^0} = (0.083 \pm 0.005) \times 10^{12}\,\mathrm{s}^{-1}$ [13], we get:

$$\mathcal{A}^{\mathrm{err}}_{\mathcal{CP}}(t) \approx -C_f \cos(\Delta m\,(t+\delta)) + S_f \sin(\Delta m\,(t+\delta))$$

and a few calculations give

$$\mathcal{A}^{\mathrm{err}}_{\mathcal{CP}}(t) = -C_f^{\mathrm{err}} \cos(\Delta m\, t) + S_f^{\mathrm{err}} \sin(\Delta m\, t)$$

with

$$\begin{aligned} C_f^{\mathrm{err}} &= -S_f \sin(\Delta m\,\delta) + C_f \cos(\Delta m\,\delta) = 0.1572 \\ S_f^{\mathrm{err}} &= S_f \cos(\Delta m\,\delta) + C_f \sin(\Delta m\,\delta) = 0.1316 \end{aligned}$$

and thus an error over C_f, S_f of

$$\left|C_f^{\text{err}} - C_f\right| = 0.007$$
$$\left|S_f^{\text{err}} - S_f\right| = 0.009$$

or a relative error of

$$\frac{\left|C_f^{\text{err}} - C_f\right|}{C_f} = 4.13\%$$
$$\frac{\left|S_f^{\text{err}} - S_f\right|}{S_f} = 6.95\%.$$

This approximated estimate highlights the impact that even small errors can have on the measured values of the $\mathcal{CP}$-violation parameters. In addition to this, the decay-time resolution has to be taken into account too, as it has a diluting effect on $\mathcal{A}_{\mathcal{CP}}(t)$. This is because the observed decay-rate distributions are the convolution of the theoretical distributions with a Gaussian with standard deviation σ_{eff} [51]. After propagating the effects of the convolution, the observed time-dependent $\mathcal{CP}$-asymmetry $\mathcal{A}_{\mathcal{CP}}^{\text{obs}}(t)$ is reduced by a multiplicative dilution factor D_σ [52]:

$$\mathcal{A}_{\mathcal{CP}}^{\text{obs}}(t) = D_\sigma \, \mathcal{A}_{\mathcal{CP}}$$

where $\mathcal{A}_{\mathcal{CP}}$ is given by Eq. (1.19) and

$$D_\sigma = e^{-(\Delta m)^2 {\sigma_{\text{eff}}}^2/2}, \tag{3.2}$$

where Δm is, as already seen, the difference between the two mass eigenstates of the neutral mesons.

As a consequence, the observed $\mathcal{CP}$ violation parameters C_f^{obs}, S_f^{obs} are rescaled in the same way:

$$C_f^{\text{obs}} = D_\sigma \, C_f$$
$$S_f^{\text{obs}} = D_\sigma \, S_f$$

where C_f, S_f are defined by Eq. (1.21).

The aim of this thesis is to estimate the decay time bias δ and the resolution σ_{eff} by analysing the prompt $J/\psi \to \mu^+\mu^-$ decays.

3.2 Data sample

3.2.1 Selection

The prompt $J/\psi \to \mu^+\mu^-$ process has been chosen for many reasons. The first is that prompt J/ψ decay instantly in the PV, as this particle has a lifetime of about 10^{-21} s [13], thus any structure in their decay time is due to the resolution of the detector. In addition to that, there is a great abundance of these decays, which gives the opportunity to perform analyses more precise from a statistical point of view. Furthermore, muons are charged particles with very

high penetrating power, making their tracks reconstructible with great precision. Finally, the two muons are a very clear signature, allowing to collect signals with little background.

The selected events come from Run 3 data, taken during October 2024. The sample has been acquired at a nominal pile-up of interaction $\mu = 5.3$. Half of the data have been acquired with a negative y component of the magnetic field, and is referred to as *data block 7*; the other half with a positive magnetic field y component and is labelled with *data block 8* (see Sec. 2.2.3). The analysis has been performed independently on both data blocks so that any asymmetry between the two magnet configurations could be highlighted.

The events are selected by the HLT2 (see Sec. 2.4.2) algorithm `Hlt2_JpsiToMuMu`, which requests strict requirements on the muon PID, a p_T above 650 MeV/c, and the invariant mass of the two muons $m(\mu^+\mu^-) \in [2950\,\text{MeV}/c^2, 3250\,\text{MeV}/c^2]$, corresponding to about $\pm 150\,\text{MeV}/c^2$ around the nominal J/ψ mass [13].

3.2.1.1 Additional cuts

Thanks to the large statistics, additional cuts have been used to improve the purity of the sample. The following conditions have been imposed:

- `Hlt1DiMuonHighMassDecision_TOS` $= 1$. This is a trigger on signal (TOS) filter based on an HLT1 selection algorithm (see Sec. 2.4.1). Both the muons must satisfy the following conditions:
  - momentum $p > 6\,\text{GeV}/c$ and $p_T > 0.5\,\text{GeV}/c$,
  - the reduced chi-squared of the reconstructed track with the associated primary vertex $\tilde{\chi}^2_{PV} < 100$,
  - the `IsMuon` algorithm [53], which identifies muons based on the number of muon stations that they traverse, gives a positive output.

  and the $\mu^+ - \mu^-$ pair must satisfy:
  - the distance of closest approach (DOCA) of the two traces $\Delta_{DOCA} < 0.2\,\text{mm}$,
  - the chi-squared of the DOCA of two muons ${\chi_{DOCA}}^2 < 25$
  - the reduced chi-squared of the vertex of the pair $\tilde{\chi}^2_{PV} < 25$
  - $m(\mu^+\mu^-) > 2.7\,\text{GeV}/c^2$
- $m(\mu^+\mu^-) \in (2950, 3240)$ MeV/c^2,
- `ProbNN_mu`$(\mu^\pm) > 0.65$, where the requirement is on the output of a neural network that quantifies the consistency of the track being a muon based on the data it has been trained on;
- `ProbNN_ghost`$(\mu^\pm) < 0.2$: same as above, but here the requirement is to have a low consistency with being a ghost track[1].

[1] A ghost track is a track that is wrongly reconstructed when certain combinations of hits mimic the pattern of a genuine track: the reconstruction algorithm interprets these as real ones, but they are artifacts arising from the reconstruction procedure and do not correspond to real particles.

All the cuts applied to the data sample are summarized in Tab. 3.1 (redundant conditions are not reported).

Variable	**Requirement**
$m(\mu^+\mu^-)$	$\in (2950, 3240)$ MeV/c^2
muon p_T	> 650 MeV/c
muon p	> 6 GeV/c
$\tilde{\chi}^2_{PV}$	< 100
`IsMuon`	`true`
Δ_{DOCA}	< 0.2 mm
${\chi_{DOCA}}^2$	< 25
$\tilde{\chi}^2_{PV}$	< 25
`ProbNN_mu`($\mu^\pm$)	> 0.65
`ProbNN_ghost`($\mu^\pm$)	< 0.2

Table 3.1: Cuts applied to select the events.

3.2.2 Binning

The dependency of the calibration on several variables has been studied. Each of the two datasets (data block 7 and data block 8) has been divided into bins, as shown in Tab. 3.2.

Variable	**# of bins**
p_T	50
η	50
ϕ	50
θ	50
# PVs	7
Δx_{PV}	10
muons direction	4

Table 3.2: Binning variables and number of bins.

The binning variables are:

1. $\boldsymbol{p_T}$, the magnitude of the J/ψ momentum component perpendicular to the beamline;
2. $\boldsymbol{\eta}$, the pseudorapidity of the J/ψ;
3. $\boldsymbol{\phi}$, the angle of the projection of the J/ψ track on the xy plane, measured counter-clockwise with respect to the positive x axis;
4. $\boldsymbol{\theta}$, the angle between the two muons;
5. the **number of PVs** in the event;

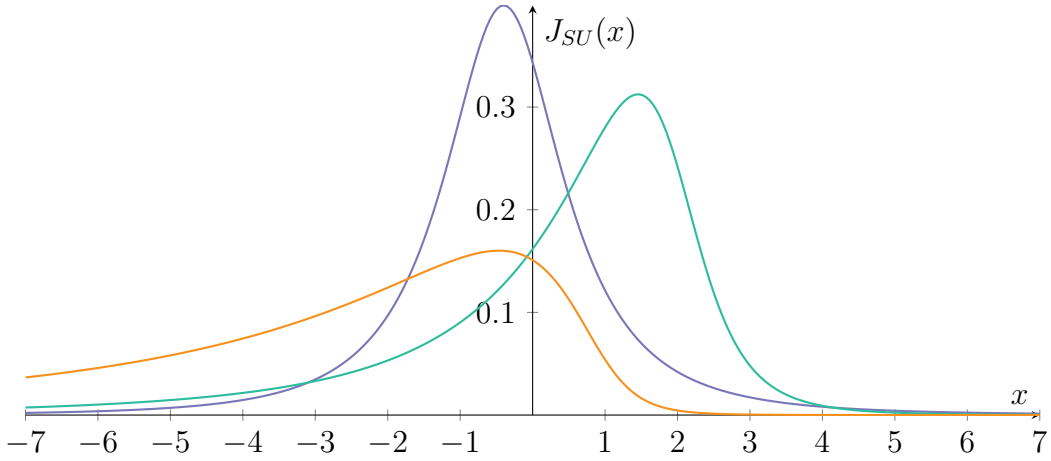

Figure 3.1: Johnson SU distribution for some parameter combinations: $\lambda = 1, \delta = 1, \xi = -0.4, \gamma = 0$ (blue); $\lambda = 1, \delta = 1, \xi = 2, \gamma = 1$ (green); $\lambda = 1, \delta = 1, \xi = 1, \gamma = 2$ (orange).

6. $\boldsymbol{\Delta x_{PV}} = |{x_{PV}}^{(A)} - {x_{PV}}^{(C)}|$, where ${x_{PV}}^{(A)}$ (${x_{PV}}^{(C)}$) is the PV x coordinate reconstructed using tracks from only the A (C) side of the VELO (see Sec. 2.2.1). This variable is a good indicator of potential misalignment between the two halves of the VELO;

7. the **muons direction**, i. e. the four possible combinations of $p_x(\mu^+), p_x(\mu^-) \gtrless 0$.

3.3 Fit strategy and model

3.3.1 Mass fit

The model used to describe the $\mu^+\mu^-$ invariant mass signal is composed of a Gaussian and a Johnson SU function [54], the latter being defined by:

$$J_{SU}(x) = \frac{\delta}{\lambda\sqrt{2\pi}} \frac{1}{\sqrt{1 + \left(\frac{x-\xi}{\lambda}\right)^2}} e^{-\frac{1}{2}\left(\gamma + \delta \sinh^{-1}\left(\frac{x-\xi}{\lambda}\right)\right)^2}$$

with the parameters $\delta, \lambda, \gamma, \xi > 0$ (see Fig. 3.1). This function is commonly used to fit invariant mass signals in B-physics [55, 56, 57]. The background, on the other hand, is modelled by an exponential function. Mass fits have been performed on every bin in order to remove combinatorial background, using the *sPlot* technique [58].

3.3.2 Decay time fit

The model for the decay time fit is composed of four functions, two Gaussians for the signal and two exponentials for the background:

- **Gaussian #1** with free mean μ and standard deviation σ_1;

- **Gaussian #2** with same mean μ and standard deviation $\sigma_2 = \alpha\,\sigma_1$, where α is a free parameter;
- **single-sided exponential** with domain in $t > 0$ and time scale τ_{SS} (left free to vary). It models the background coming from non-prompt J/ψ, typically from $B \to J/\psi\, X$ decays;
- **double-sided exponential** with a free time scale τ_{DS}, that models the background of J/ψ associated with a wrong PV.

Both the single-sided and the double-sided exponentials are convoluted with the resolution of the signal model (i. e. the sum of the two Gaussians).

It is quite immediate to understand that the decay time bias is μ. The decay time resolution σ_{eff} can be computed according to

$$e^{-(\Delta m)^2 {\sigma_{\text{eff}}}^2/2} = D_\sigma = f_1\, e^{-(\Delta m)^2 {\sigma_1}^2/2} + (1 - f_1)\, e^{-(\Delta m)^2 {\sigma_2}^2/2}$$

and thus

$$\sigma_{\text{eff}} = \sqrt{-\frac{2\ln(D_\sigma)}{(\Delta m)^2}}$$

where f_1 is the fraction of the signal of the first Gaussian. By recalling Eq. (3.2) one can interpret σ_{eff} as the standard deviation of a Gaussian function causing the same dilution of the double-Gaussian model used in the fit.

3.4 Results

The model presented in Sec. 3.3.2 has been adapted to the background-subtracted decay-time distributions of every bin of every binning variable, using the data analysis framework RooFit. The model has been applied with an unbinned maximum-likelihood fit. The model describes well the data, as it can be seen in Figs. 3.3 and 3.4.

Then, for each binning variable, a weighted average of the fit parameters has been calculated. The averaged results are expected to be the same for all binning variables, with discrepancies indicating potential systematic uncertainties arising from the fitting model.

The results are listed in Tab. 3.3; the weighted means of the bias and σ_{eff} are also depicted in Fig. 3.2. The fraction of non-prompt J/ψ and wrong PV J/ψ are, respectively, f_{SS} and f_{DS}; the fraction of signal events is thus $1 - f_{SS} - f_{DS}$. As it can be seen, the averaged bias and resolution have very small variations depending on the binning variable. Their means are:

$$\delta = (-3.2 \pm 0.3)\,\text{fs}$$
$$\sigma_{\text{eff}} = (50.4 \pm 0.3)\,\text{fs},$$

where the statistical error reported is expected to be negligible compared to the systematic one, which is currently under evaluation.

Generally speaking, a decay-time bias of around $-3\,\text{fs}$ has been found; in data block 8 this value is systematically lower, by around 7%, compared to data block 7. The resolution is

Binning variable	**Bias** (fs)	σ_{eff} (fs)	τ_{SS} (ps)	τ_{DS} (ps)	f_{SS}	f_{DS}
Δx_{PV}	−3.09(7)	50.42(6)	1.378(7)	0.587(10)	0.1279(5)	0.0236(4)
	−3.29(7)	50.66(7)	1.383(7)	0.585(10)	0.1277(5)	0.0242(4)
η	−3.00(9)	50.21(9)	1.39(2)	0.385(11)	0.1277(7)	0.0256(8)
	−3.18(10)	50.49(10)	1.39(2)	0.392(7)	0.1274(7)	0.0256(9)
muons side	−3.00(4)	50.37(4)	1.382(4)	0.545(6)	0.1280(3)	0.0238(3)
	−3.17(5)	50.63(4)	1.386(5)	0.550(6)	0.1280(3)	0.0239(3)
# PVs	−3.09(6)	50.41(5)	1.375(6)	0.588(14)	0.1284(4)	0.0236(3)
	−3.29(6)	50.73(5)	1.381(6)	0.596(19)	0.1277(4)	0.0240(3)
ϕ	−3.07(9)	50.40(8)	1.378(9)	0.585(12)	0.1282(6)	0.0237(5)
	−3.25(9)	50.69(8)	1.378(9)	0.587(13)	0.1280(7)	0.0236(5)
p_T	−3.15(9)	49.83(9)	1.389(12)	0.397(14)	0.1288(6)	0.0265(7)
	−3.36(10)	50.24(9)	1.387(13)	0.414(15)	0.1276(7)	0.0274(8)
θ	−3.02(9)	50.38(8)	1.379(9)	0.588(15)	0.1286(6)	0.0236(5)
	−3.20(10)	50.67(9)	1.380(10)	0.591(17)	0.1284(7)	0.0235(5)

Table 3.3: Weighted mean of fit parameters over the different binning variables. The upper value is relative to data block 7, the lower to data block 8.

about 50 fs; here, data block 8 values are higher, by around 0.5%. As a comparison, bias and resolution values for Run 2 were, respectively, ≈ -3 fs and ≈ 40 fs. The other fit parameters are compatible among the different binning variables in each data block, with the exception of τ_{DS} and f_{DS} in η and p_T binning. This is somehow expected, as the probability of wrongly associating the J/ψ to a PV depends on these variables given the forward acceptance of LHCb. Interesting dependences of the parameters on the binning variables have been found, as it will be discussed in the next sections.

3.4.1 p_T binning

A strong dependence of the wrong-PV component from p_T was expected, as the angular distance between two different PVs gets bigger as p_T increases. This has been, in fact, observed, as it can be seen in the f_{DS} vs p_T graph in Fig. 3.5. This is also evident from the two decay time fits in Fig. 3.6. The decay time bias increases with growing p_T, while σ_{eff} decreases (see Fig. 3.7).

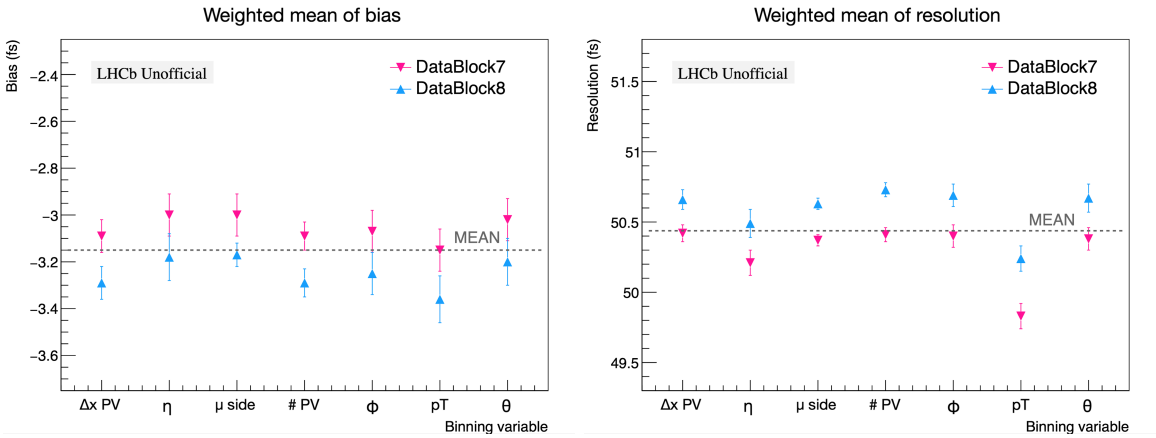

Figure 3.2: Bias and resolution for the different binning variables. The mean over all 14 values is also shown.

3.4.2 η binning

As the pseudorapidity η is related to the angle of the J/ψ with respect to the beam axis, a dependence of f_{DS} on η is expected too; but in this case, the bigger η, the bigger the chance of a wrong PV association. This is confirmed by the results, as it can be seen in Fig. 3.8.

As shown in Fig. 3.9, the bias starts at 4 fs, has a minimum in $\eta = 3.5$, and then grows again reaching -2 fs; the resolution grows from 47 fs to 58 fs, following a curve that is steeper for $4 < \eta < 5$. The curve is similar to a sigmoid or $\arctan(\eta)$.

3.4.3 ϕ binning

An interesting, non-symmetrical pattern arises for the decay time bias, as shown in Fig. 3.10. The two relative maxima are for $\phi \approx \pm\pi/2$, i. e. the two separation points between the two sides (C side and A side) of the VELO (see Sec. 2.2.1). The resolution has a less significant dependence on ϕ, as well as f_{DS} (Fig. 3.11) and f_{SS}. These patterns may reflect some left-right misalignments of the VELO halves.

3.4.4 θ binning

The decay time bias decreases with growing θ, from 0 to -6 fs, while σ_{eff} grows from 40 to 63 fs (see Fig. 3.12). In data block 7, the bias and resolution are, respectively, systematically higher and lower in most bins.

3.4.5 # PVs binning

For this variable binning, for the first time, there is no clear dependence on the bias, while the resolution is inversely correlated to the number of PVs, as shown in Fig. 3.13. The fraction of events with wrong-PV association, as expected, grows with the number of PVs, as it can be seen in Fig. 3.14.

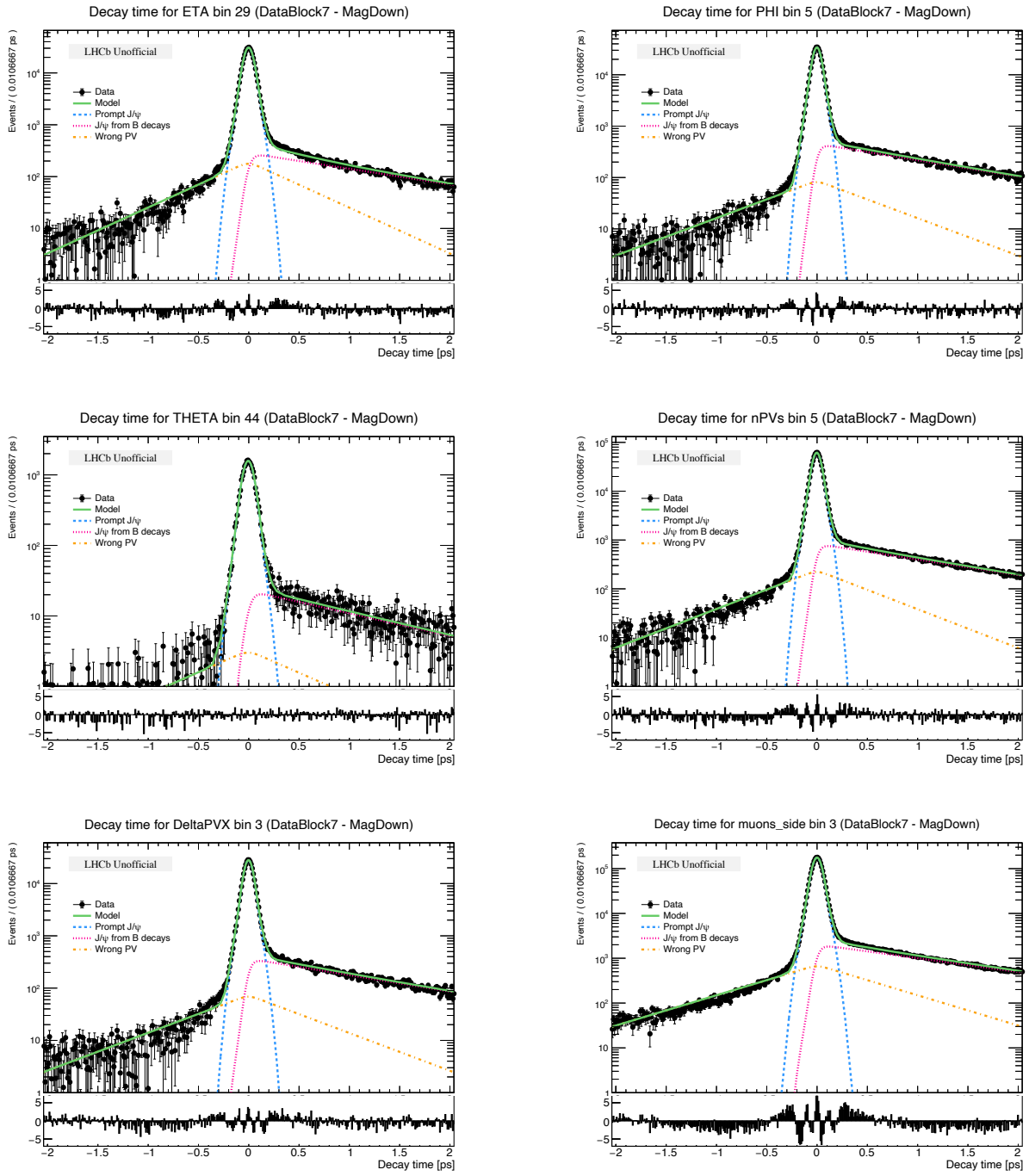

Figure 3.3: Decay-time data and its fit on some bins. Events were collected in data block 7.

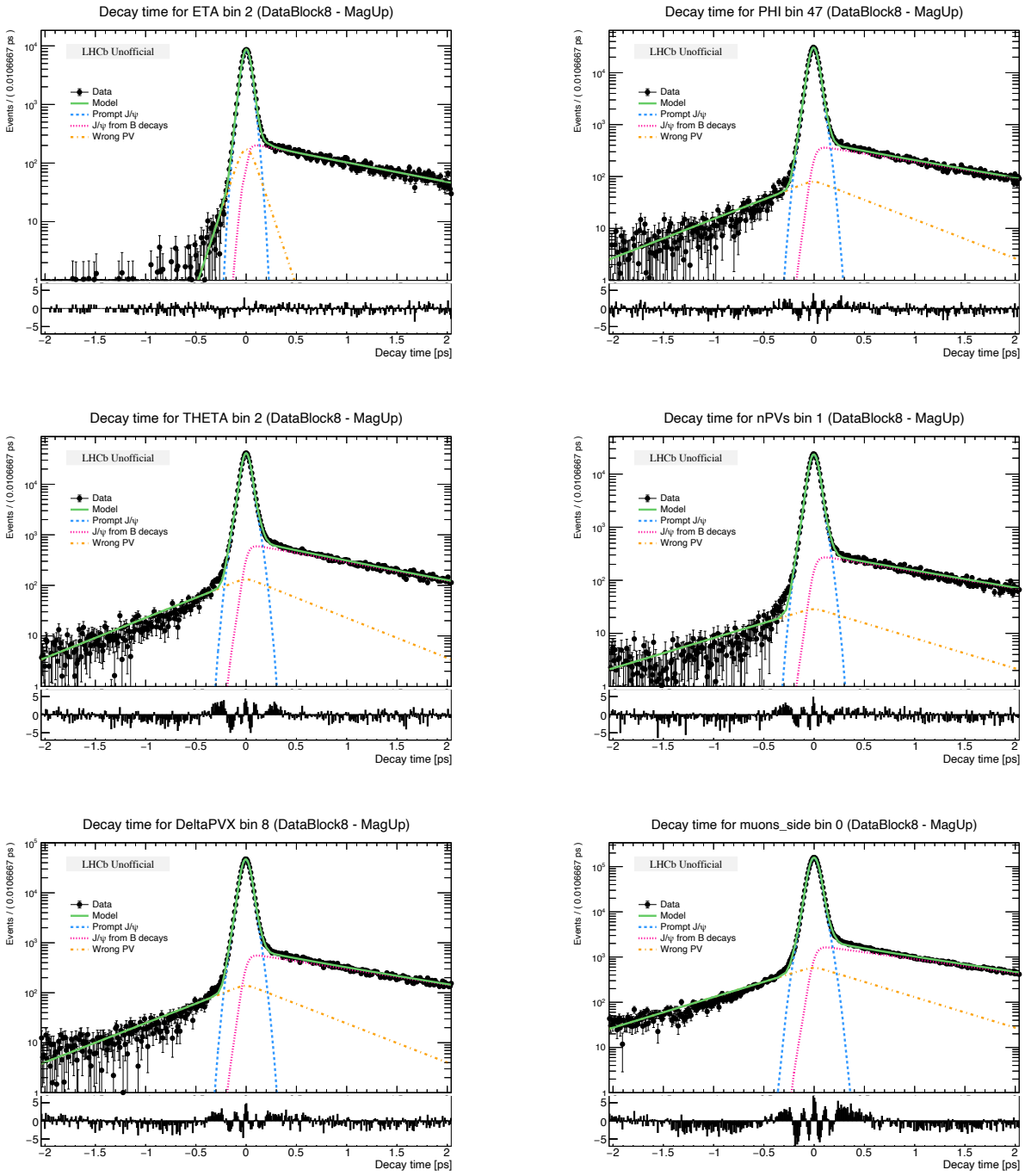

Figure 3.4: Decay-time data and its fit on some bins. Events were collected in data block 8.

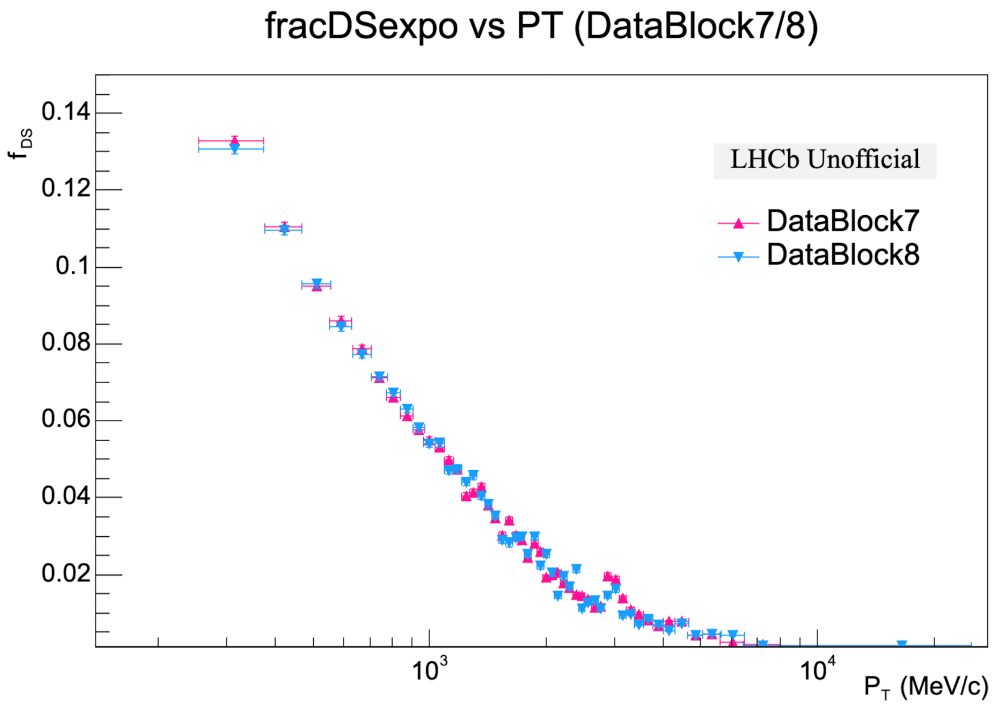

Figure 3.5: Fraction of wrong PV events as a function of p_T.

3.4.6 Δx_{PV} binning

The bias shows a clear dependence on Δx_{PV}, going from -2 fs to -5 fs. Interestingly, it is not 0 when $\Delta x_{PV} = 0$, a hint that the bias could not depend only on the VELO misalignment, but on a more general effect of the tracking system. The effective resolution, on the other hand, is around 50 fs and varies little. Both graphs are shown in Fig. 3.15.

3.4.7 Muons side binning

Both the bias and the resolution depend on which side of the detector the two muons are directed to (i. e. the muon is detected on the positive or negative x side of the detector), as shown in Fig. 3.16. Very interestingly, the bias is sharply different between the two data blocks (which correspond to different magnet polarities) when the two muons go to opposite sides; while there is no difference when they both go to the positive or negative x side. This pattern is associated with the curvature direction of the two muons. When both the curvatures are towards the beam pipe, the bias is smaller, whereas when the curvatures are towards the outer part of the detector, the bias is larger. This effect too points to a more general misalignment of the detector and not to a misalignment of the VELO only.

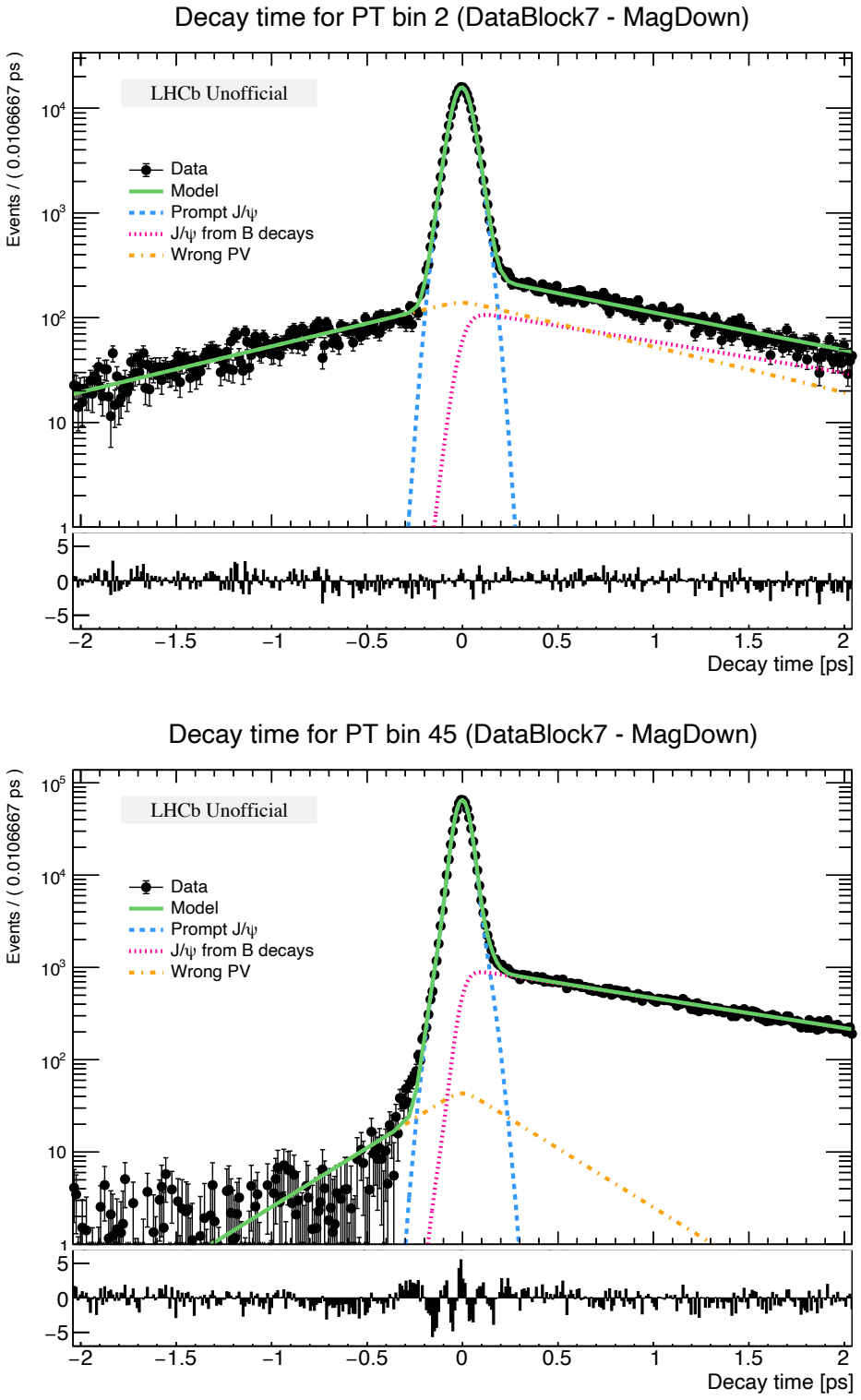

Figure 3.6: Decay time fits for p_T bin 2 (low p_T) and bin 45 (high p_T). Note how the wrong PV component is much smaller for high p_T.

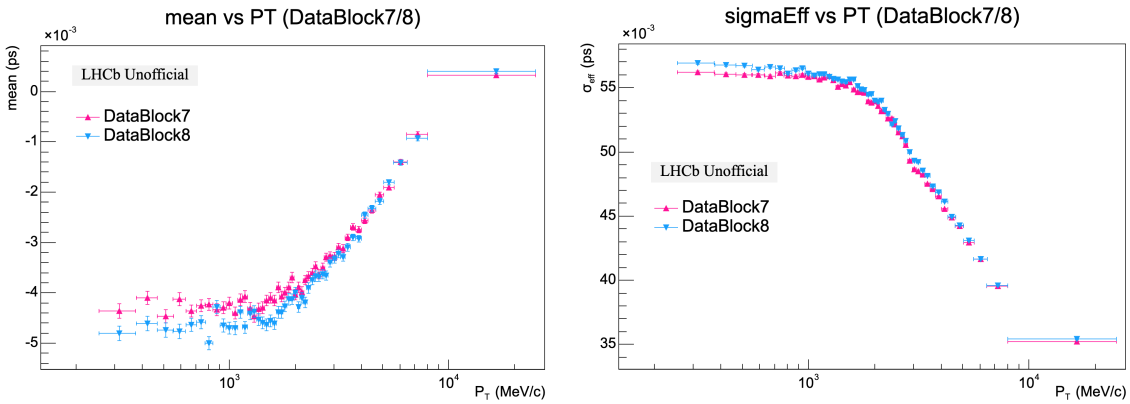

Figure 3.7: Bias and resolution as a function of p_T

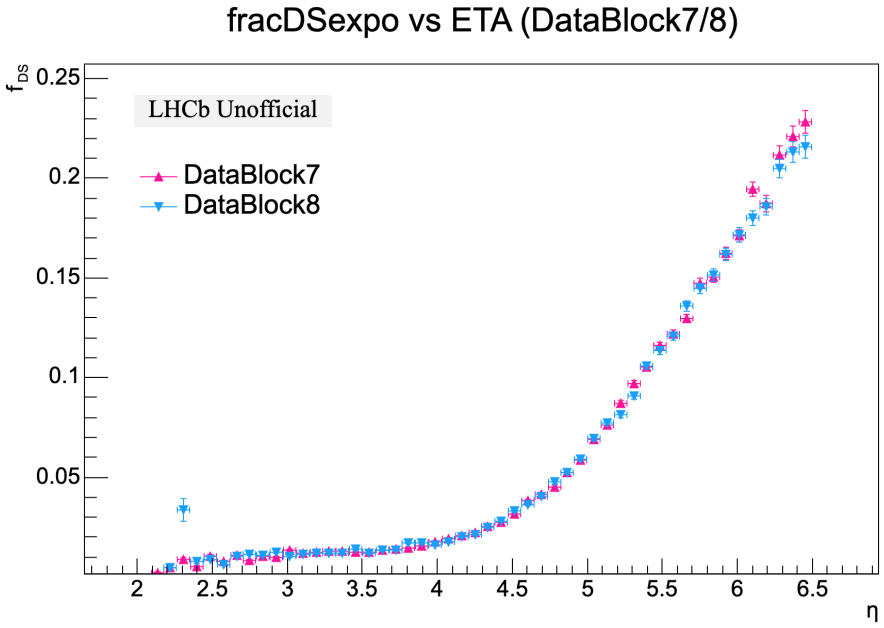

Figure 3.8: Fraction of wrong PV events as a function of η.

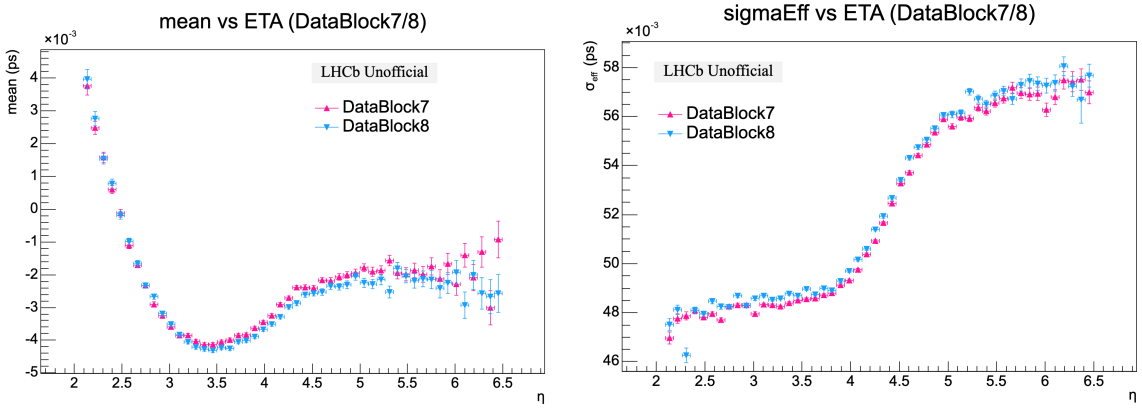

Figure 3.9: Bias and resolution as a function of η.

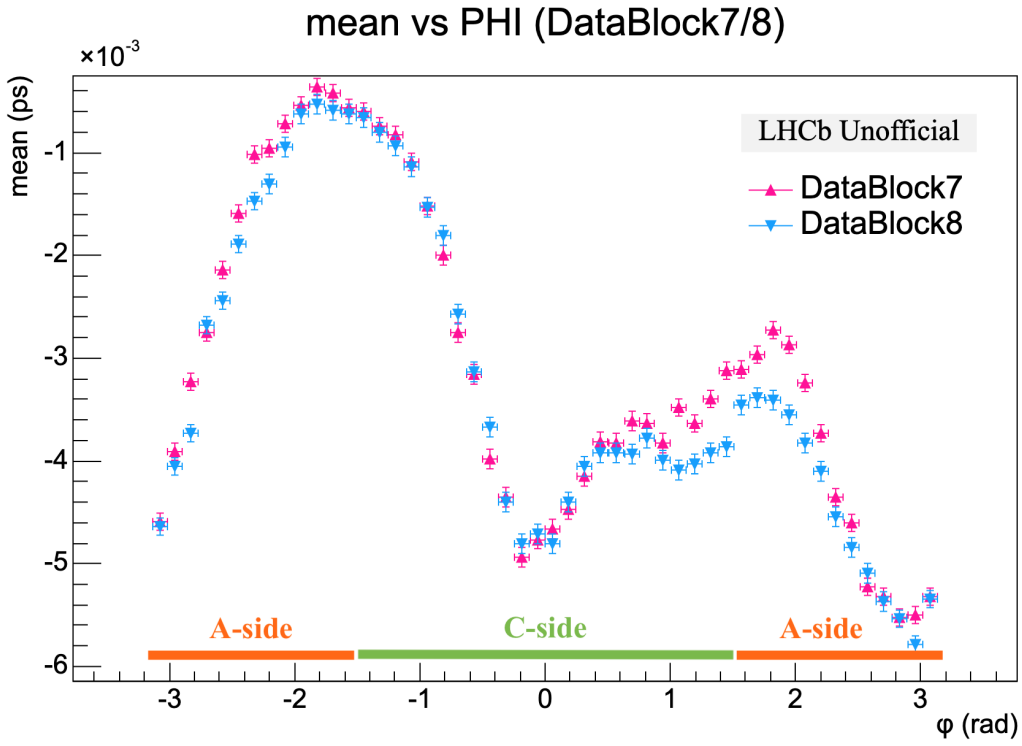

Figure 3.10: Decay time bias as a function of ϕ. The domain intervals corresponding to the two sides of the VELO are shown.

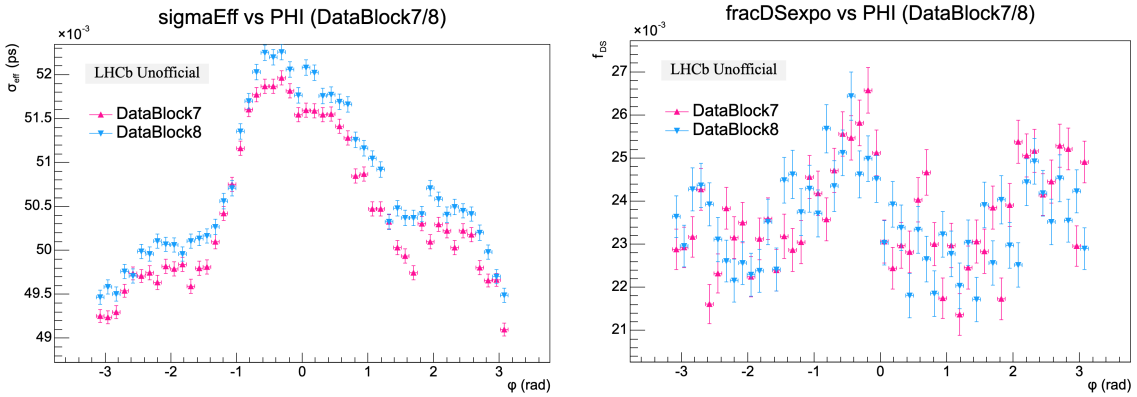

Figure 3.11: Resolution and fraction of wrong PV events as a function of ϕ; the latter does not show a significant dependence.

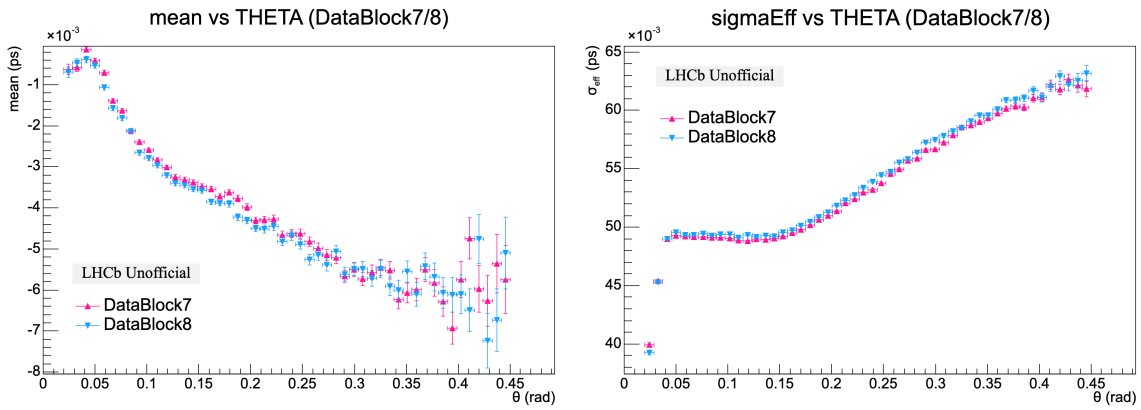

Figure 3.12: Bias and resolution as a function of θ.

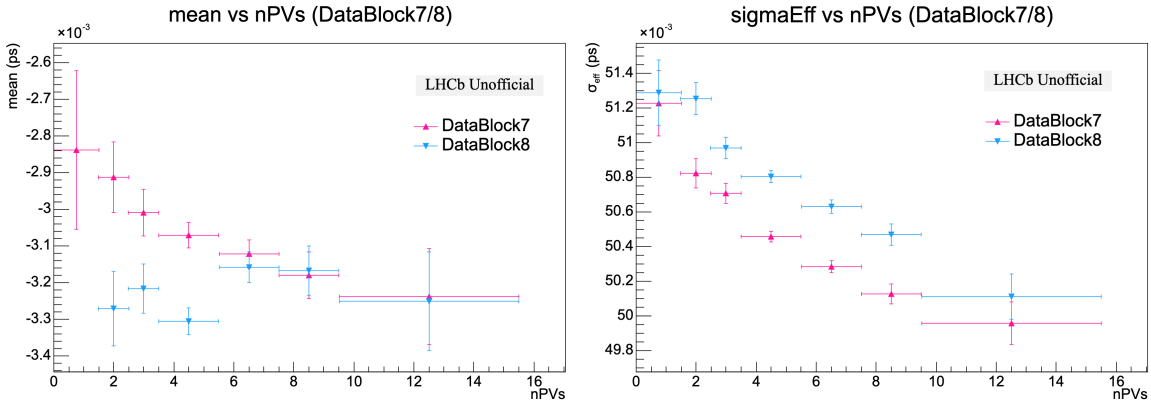

Figure 3.13: Bias and resolution as a function of # PVs.

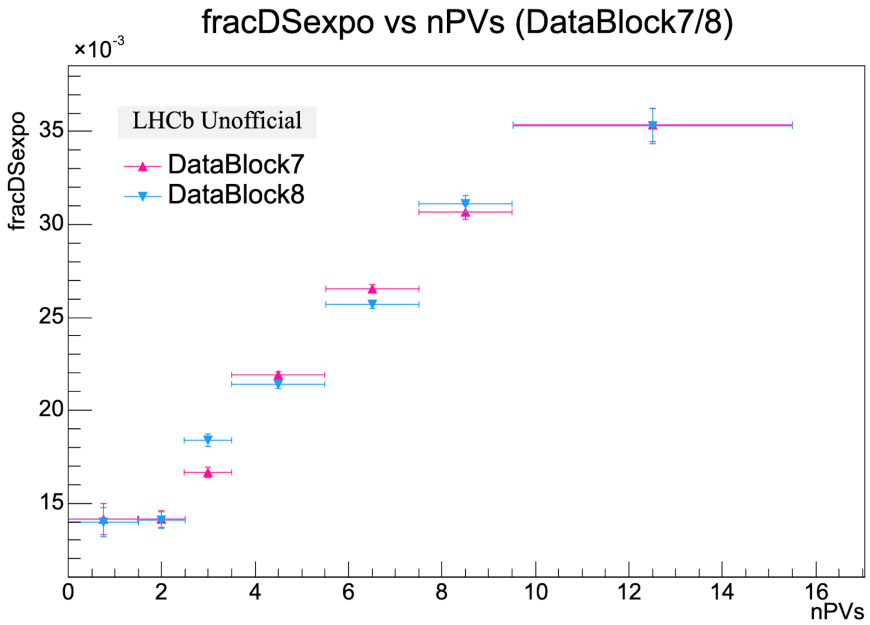

Figure 3.14: f_{DS} as a function of # PVs.

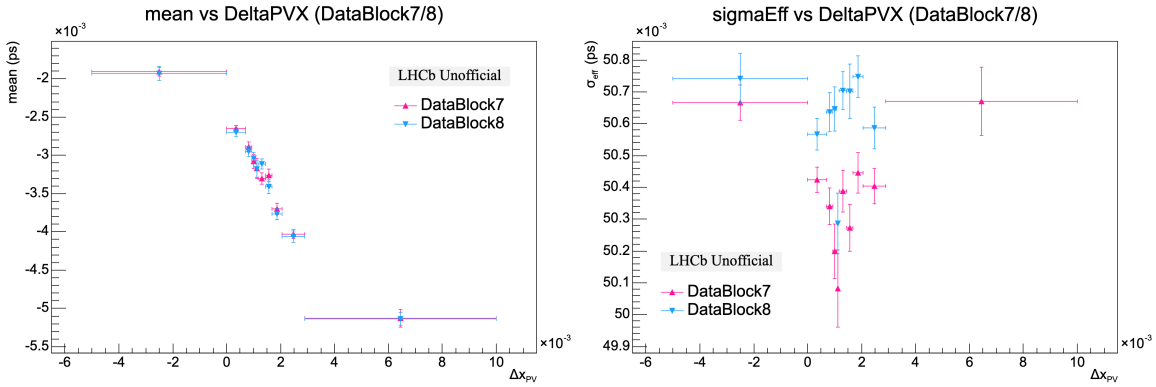

Figure 3.15: Bias and resolution as a function of Δx_{PV}, in mm. Note how the bias is different from 0 when $\Delta x_{PV} = 0$.

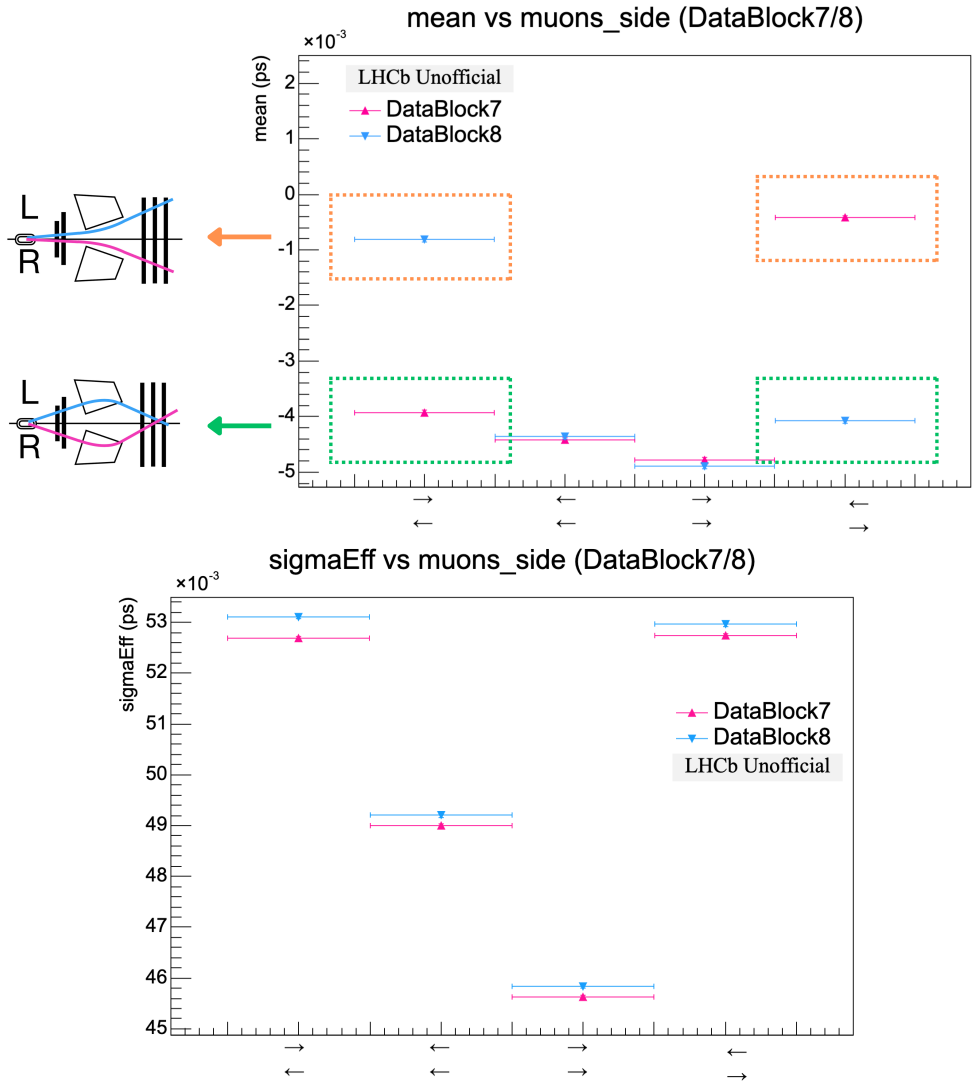

Figure 3.16: Bias and resolution for different combination of sides of muon tracks. The upper arrow is relative to μ^+, the lower to μ^-.

Conclusions

In the first chapter, the main features of the Standard Model, flavour mixing and $\mathcal{CP}$-violation mechanisms are discussed. In the second one, the LHCb detector is presented through its main components after the upgrade. In the third chapter, a thorough calibration of the decay time measured with the LHCb Upgrade I detector during Run 3 is reported. A precise calibration is crucial, as it has relevant effects on the measurements of $\mathcal{CP}$-violation parameters.

A decay-time bias of the order of a femtosecond, if neglected, causes a shift in B_s^0-meson time-dependent $\mathcal{CP}$-violation parameters of about 5%, which is comparable to the statistical uncertainty already achieved with the Run 2 sample. The bigger sample size of Run 3, due to a fivefold increase in the instantaneous luminosity, makes the proper calibration of this effect even more important.

Moreover, the effects of the resolution σ_{eff} dilute the amplitude of the time-dependent $\mathcal{CP}$ asymmetry by a multiplicative factor

$$D_\sigma = e^{-(\Delta m)^2 {\sigma_{\text{eff}}}^2/2}$$

which, in the case of $B_s^0 \to K^+K^-$ (one of the main decays studied at LHCb to measure $\mathcal{CP}$-violation parameters) is about 75%.

To precisely calibrate the decay-time measurement, prompt $J/\psi \to \mu^+\mu^-$ decays have been chosen, due to their instant decay, abundance, and clear signature. The data refer to data block 7 (LHCb magnet polarity $\uparrow$) and 8 (magnet polarity $\downarrow$), collected by LHCb during October 2024.

The sample has been divided into different bins depending on seven variables: p_T, η, ϕ, θ, the number of PVs, Δx_{PV} and the muons direction ($p_x \gtrless 0$). An invariant mass fit with a Gaussian and a Johnson SU function for the signal and an exponential for the background has been performed on every bin in order to subtract the combinatorial background. Then, a decay time fit with two Gaussians (signal), a double-sided exponential function (background due to wrong PV association), and a single-sided exponential function (background due to non-prompt J/ψ) has been performed. In addition to the bias and resolution, the dependences of the fraction of the two background events and the two time scales of the exponential functions on the binning variable have been examined.

The bias δ and the resolution σ_{eff} have been found to be

$$\delta = (-3.2 \pm 0.3)\,\text{fs},$$
$$\sigma_{\text{eff}} = (50.4 \pm 0.3)\,\text{fs},$$

where the statistical error is not very significant as it is expected to be negligible compared to the systematic one, which is currently under evaluation.

The bias shows a clear dependence on every binning variable except for the number of PVs, while the resolution depends on all of them. Some interesting results are the fact that the bias is non-zero when the two halves of the VELO are expected to be perfectly aligned in x (i. e. when $\Delta x_{PV} = 0$); the striking difference in the bias between data blocks 7 and 8 depending on the curvature direction of the two muons; and an asymmetric pattern of the bias as a function of ϕ with relative maxima for the ϕ values corresponding to the separation point between the two sides of the VELO.

All these effects point in the direction of a general, despite very small, misalignment of the tracking system of LHCb Upgrade I. At the moment of writing this thesis, the work contained in it is being discussed with the tracking and alignment experts of the experiment to find the source of the observed behaviour. The continuation of this work will also include the transformation of the calibrated bias and resolution in those expected for $B_s^0 \to K^+K^-$ decays.

Thanks to the massive enhancements of the detector components, luminosity, and triggering system, LHCb upgrade I is expected to measure with unprecedented precision $\mathcal{CP}$-violation parameters and deepen our understanding of many fundamental and intriguing aspects of our universe, including the baryonic asymmetry. In order to achieve this goal, a thorough understanding and calibration of the detector are crucial; the hope is for this work to be a small step in this direction.

References

[1] Y. Fukuda et al. "Evidence for Oscillation of Atmospheric Neutrinos". In: *Phys. Rev. Lett.* 81 (8 1998), pp. 1562–1567. DOI: 10.1103/PhysRevLett.81.1562. URL: https://link.aps.org/doi/10.1103/PhysRevLett.81.1562.

[2] X. Fan et al. "Measurement of the Electron Magnetic Moment". In: *Phys. Rev. Lett.* 130 (7 2023), p. 071801. DOI: 10.1103/PhysRevLett.130.071801. URL: https://link.aps.org/doi/10.1103/PhysRevLett.130.071801.

[3] M. D. Schwartz. *Quantum Field Theory and the Standard Model*. Cambridge University Press, 2014.

[4] S. L. Glashow. "Partial-symmetries of weak interactions". In: *Nuclear Physics* 22.4 (1961), pp. 579–588. ISSN: 0029-5582. DOI: https://doi.org/10.1016/0029-5582(61)90469-2.

[5] S. Weinberg. "A Model of Leptons". In: *Phys. Rev. Lett.* 19 (21 1967), pp. 1264–1266. DOI: 10.1103/PhysRevLett.19.1264. URL: https://link.aps.org/doi/10.1103/PhysRevLett.19.1264.

[6] A. Salam and J. C. Ward. "Weak and electromagnetic interactions". In: *Il Nuovo Cimento (1955-1965)* 11.4 (Feb. 1, 1959), pp. 568–577. ISSN: 1827-6121. DOI: 10.1007/BF02726525. URL: https://doi.org/10.1007/BF02726525.

[7] T. Nakano and K. Nishijima. "Charge Independence for V-particles*". In: *Progress of Theoretical Physics* 10.5 (Nov. 1953), pp. 581–582. ISSN: 0033-068X. DOI: 10.1143/PTP.10.581. eprint: https://academic.oup.com/ptp/article-pdf/10/5/581/5364926/10-5-581.pdf. URL: https://doi.org/10.1143/PTP.10.581.

[8] The LHCb collaboration. "Observation of structure in the J/ψ-pair mass spectrum". In: *Science Bulletin* 65.23 (2020), pp. 1983–1993. ISSN: 20959273. DOI: 10.1016/j.scib.2020.08.032. arXiv: 2006.16957[hep-ex]. URL: http://arxiv.org/abs/2006.16957.

[9] The LHCb collaboration. "Observation of a Narrow Pentaquark State, $P_c(4312)^+$, and of the Two-Peak Structure of the $P_c(4450)^+$". In: *Physical Review Letters* 122.22 (2019). DOI: 10.1103/physrevlett.122.222001.

[10] N. Cabibbo. "Unitary Symmetry and Leptonic Decays". In: *Phys. Rev. Lett.* 10 (12 1963), pp. 531–533. DOI: 10.1103/PhysRevLett.10.531.

[11] M. Kobayashi and T. Maskawa. "CP-Violation in the Renormalizable Theory of Weak Interaction". In: *Progress of Theoretical Physics* 49.2 (1973), pp. 652–657. ISSN: 0033-068X. DOI: 10.1143/PTP.49.652. URL: https://doi.org/10.1143/PTP.49.652.

[12] L.-L. Chau and W.-Y. Keung. "Comments on the Parametrization of the Kobayashi-Maskawa Matrix". In: *Phys. Rev. Lett.* 53 (19 1984), pp. 1802–1805. DOI: 10.1103/PhysRevLett.53.1802. URL: https://link.aps.org/doi/10.1103/PhysRevLett.53.1802.

[13] S. Navas et al. "Review of particle physics". In: *Phys. Rev. D* 110.3 (2024), p. 030001. DOI: 10.1103/PhysRevD.110.030001.

[14] L. Wolfenstein. "Parametrization of the Kobayashi-Maskawa Matrix". In: *Phys. Rev. Lett.* 51 (21 1983), pp. 1945–1947. DOI: 10.1103/PhysRevLett.51.1945.

[15] M. Bona et al. "New UTfit analysis of the unitarity triangle in the Cabibbo–Kobayashi–Maskawa scheme". In: *Rendiconti Lincei. Scienze Fisiche e Naturali* 34.1 (Mar. 1, 2023), pp. 37–57. ISSN: 1720-0776. DOI: 10.1007/s12210-023-01137-5. URL: https://doi.org/10.1007/s12210-023-01137-5.

[16] CKMfitter Group, J. Charles, et al. "CP violation and the CKM matrix: Status and prospects". In: *Eur. Phys. J. C* 41 (2005), pp. 1–131. arXiv: hep-ph/0406184 [hep-ph]. URL: http://ckmfitter.in2p3.fr.

[17] E. Noether. "Invariant variation problems". In: *Transport Theory and Statistical Physics* 1.3 (1971), pp. 186–207. DOI: 10.1080/00411457108231446. eprint: https://doi.org/10.1080/00411457108231446. URL: https://doi.org/10.1080/00411457108231446.

[18] G. Luders. "On the Equivalence of Invariance under Time Reversal and under Particle-Antiparticle Conjugation for Relativistic Field Theories". In: *Kong. Dan. Vid. Sel. Mat. Fys. Med.* 28N5.5 (1954), pp. 1–17.

[19] C. S. Wu et al. "Experimental Test of Parity Conservation in Beta Decay". In: *Phys. Rev.* 105 (4 1957), pp. 1413–1415. DOI: 10.1103/PhysRev.105.1413. URL: https://link.aps.org/doi/10.1103/PhysRev.105.1413.

[20] J. H. Christenson et al. "Evidence for the 2π Decay of the K_2^0 Meson". In: *Phys. Rev. Lett.* 13 (1964), pp. 138–140. DOI: 10.1103/PhysRevLett.13.138.

[21] The LHCb collaboration. "Observation of CP violation in two-body $B^0_{(s)}$-meson decays to charged pions and kaons". In: *Journal of High Energy Physics* 3 (Mar. 8, 2021), p. 75. ISSN: 1029-8479. DOI: 10.1007/JHEP03(2021)075. URL: https://doi.org/10.1007/JHEP03(2021)075.

[22] G. Cowan. "Measurements of CP violation in B mixing through $B \to J/\psi X$ decays at LHCb". In: *Proceedings of Science* (Oct. 2015). DOI: 10.48550/arXiv.1510.03990.

[23] The LHCb Collaboration. "The LHCb Detector at the LHC". In: *Journal of Instrumentation* 3.08 (2008), S08005. DOI: 10.1088/1748-0221/3/08/S08005. URL: https://dx.doi.org/10.1088/1748-0221/3/08/S08005.

[24] The LHCb Collaboration. "The LHCb Upgrade I". In: *Journal of Instrumentation* 19.05 (May 23, 2024). DOI: 10.1088/1748-0221/19/05/P05065. URL: https://dx.doi.org/10.1088/1748-0221/19/05/P05065.

[25] E. Graverini. "Luminosity at LHCb in Run 3". In: *PoS* ICHEP2022 (2022), p. 679. DOI: 10.22323/1.414.0679. arXiv: 2211.12405 [hep-ex].

[26] F. Follin and D. Jacquet. "Implementation and experience with luminosity levelling with offset beam". In: *ICFA Mini-Workshop on Beam-Beam Effects in Hadron Colliders*. 2014, pp. 183–187. DOI: 10.5170/CERN-2014-004.183. arXiv: 1410.3667 [physics.acc-ph].

[27] The LHCb Collaboration. "LHCb detector performance". In: *International Journal of Modern Physics A* 30.07 (2015), p. 1530022. DOI: 10.1142/S0217751X15300227. eprint: https://doi.org/10.1142/S0217751X15300227. URL: https://doi.org/10.1142/S0217751X15300227.

[28] A. A. Alves Jr. et al. "The LHCb Detector at the LHC". In: *JINST* 3 (2008), S08005. DOI: 10.1088/1748-0221/3/08/S08005.

[29] The LHCb Collaboration. *LHCb PLUME: Probe for LUminosity MEasurement*. Tech. rep. CERN, 2021. DOI: 10.17181/CERN.WLU0.M37F.

[30] C. Ilgner et al. *The Beam Conditions Monitor of the LHCb Experiment*. 2010. arXiv: 1001.2487 [physics.ins-det]. URL: https://arxiv.org/abs/1001.2487.

[31] V. Pugatch et al. *Metal Foil Detectors assembly for the beam and background monitoring in the LHCb experiment*. 2025. arXiv: 2503.13629 [hep-ex]. URL: https://arxiv.org/abs/2503.13629.

[32] C. Barschel. "Precision luminosity measurement at LHCb with beam-gas imaging". Presented 05 Mar 2014. RWTH Aachen U., 2014. URL: https://cds.cern.ch/record/1693671.

[33] The LHCb Collaboration. *LHCb VELO Upgrade Technical Design Report*. Tech. rep. CERN, 2013. DOI: 10.17181/CERN.4DGI.MZN4. URL: https://cds.cern.ch/record/1624070.

[34] The LHCb Collaboration. *LHCb Tracker Upgrade Technical Design Report*. Tech. rep. CERN, 2014. DOI: 10.17181/CERN.OOOE.9O9T. URL: https://cds.cern.ch/record/1647400.

[35] S. Amato et al. *LHCb magnet: Technical Design Report*. Technical design report. LHCb. Geneva: CERN, 2000. DOI: 10.17181/CERN.MCVC.Q12G. URL: https://cds.cern.ch/record/424338.

[36] J. Andre et al. "Status of the LHCb magnet system". In: *IEEE Transactions on Applied Superconductivity* 12.1 (2002), pp. 366–371. DOI: 10.1109/TASC.2002.1018421.

[37] B. K. Jashal. "Standalone track reconstruction and matching algorithms for GPU-based High level trigger at LHCb". In: *CERN* (2022). URL: https://cds.cern.ch/record/2826068.

[38] J. V. Jelley. *Cerenkov Radiation And Its Applications*. Pergamon Press, 1958. 331 pp. URL: http://archive.org/details/cerenkovradiatio030980mbp.

[39] R. W. Forty and O. Schneider. *RICH pattern recognition*. Tech. rep. Geneva: CERN, 1998. URL: https://cds.cern.ch/record/684714.

[40] R. Antunes-Nobrega, A. França-Barbosa, and I. Bediaga. *LHCb reoptimized detector design and performance: Technical Design Report*. Technical design report. LHCb. Geneva: CERN, 2003. URL: https://cds.cern.ch/record/630827.

[41] S. Amato et al. *LHCb calorimeters: Technical Design Report*. Technical design report. LHCb. Geneva: CERN, 2000. URL: https://cds.cern.ch/record/494264.

[42] S. Barsuk et al. *Design and construction of electromagnetic calorimeter for LHCb experiment*. Tech. rep. Geneva: CERN, 2000. URL: https://cds.cern.ch/record/691508.

[43] R. Djeliadine, O. Iouchtchenko, and V. F. Obraztsov. *LHCb hadron trigger and Hcal cell size and length optimization*. Tech. rep. Geneva: CERN, 1999. URL: https://cds.cern.ch/record/691688.

[44] P. R. Barbosa-Marinho, I. Bediaga, and G. Cernicchiaro. *LHCb muon system: Technical Design Report*. Technical design report. LHCb. Geneva: CERN, 2001. URL: https://cds.cern.ch/record/504326.

[45] S. C. Brown and E. H. Holt. "Introduction to Electrical Discharges in Gases". In: *American Journal of Physics* 36.9 (Sept. 1, 1968), pp. 854–854. ISSN: 0002-9505, 1943-2909. DOI: 10.1119/1.1975174. URL: https://pubs.aip.org/ajp/article/36/9/854/1043070/Introduction-to-Electrical-Discharges-in-Gases (visited on 03/31/2025).

[46] R. Aaij et al. "Allen: A high level trigger on GPUs for LHCb". In: *Comput. Softw. Big Sci.* 4.1 (2020), p. 7. DOI: 10.1007/s41781-020-00039-7. arXiv: 1912.09161 [physics.ins-det].

[47] R. E. Kalman. "A New Approach to Linear Filtering and Prediction Problems". In: *Journal of Basic Engineering* 82.1 (Mar. 1960), pp. 35–45. ISSN: 0021-9223. DOI: 10.1115/1.3662552. eprint: https://asmedigitalcollection.asme.org/fluidsengineering/article-pdf/82/1/35/5518977/35_1.pdf. URL: https://doi.org/10.1115/1.3662552.

[48] R. Aaij et al. "A comprehensive real-time analysis model at the LHCb experiment". In: *Journal of Instrumentation* 14.04 (2019), P04006. DOI: 10.1088/1748-0221/14/04/P04006. URL: https://dx.doi.org/10.1088/1748-0221/14/04/P04006.

[49] The LHCb Collaboration. *Computing Model of the Upgrade LHCb experiment*. Tech. rep. Geneva: CERN, 2018. DOI: 10.17181/CERN.Q0P4.57ON. URL: https://cds.cern.ch/record/2319756.

[50] The LHCb Collaboration. *RTA and DPA dataflow diagrams for Run 1, Run 2, and the upgraded LHCb detector*. Tech. rep. CERN, 2020. URL: https://cds.cern.ch/record/2730181.

[51] D. Manuzzi. "Measurement of $\mathcal{CP}$ violation with $B^0_{(s)} \to h^+h'^-$ decays, $|V_{cb}|$ with $B^0_s \to D_s^{(*)-}\mu^+\nu_\mu$ decays, and simulation and characterisation of the LHCb Upgrade II ECAL". PhD thesis. Università di Bologna, 2022.

[52] H.-G. Moser and A. Roussarie. "Mathematical methods for B^0-$\overline{B}^0$ oscillation analyses". In: *Nuclear Instruments and Methods in Physics Research Section A: Accelerators, Spectrometers, Detectors and Associated Equipment* 384.2 (1997), pp. 491–505. ISSN: 0168-9002. DOI: https://doi.org/10.1016/S0168-9002(96)00887-X. URL: https://www.sciencedirect.com/science/article/pii/S016890029600887X.

[53] L. Anderlini et al. "Muon identification for LHCb Run 3". In: *Journal of Instrumentation* 15.12 (2020), T12005. DOI: 10.1088/1748-0221/15/12/T12005. URL: https://dx.doi.org/10.1088/1748-0221/15/12/T12005.

[54] N. L. Johnson. "Systems of Frequency Curves Generated by Methods of Translation". In: *Biometrika* 36.1/2 (1949), pp. 149–176. ISSN: 00063444, 14643510. URL: http://www.jstor.org/stable/2332539 (visited on 04/17/2025).

[55] The LHCb Collaboration. "Precise determination of the B_s^0-$\overline{B}_s^0$ oscillation frequency". In: *Nature Physics* 18.1 (Jan. 2022). Publisher: Nature Publishing Group, pp. 1–5. ISSN: 1745-2481. DOI: 10.1038/s41567-021-01394-x. URL: https://www.nature.com/articles/s41567-021-01394-x (visited on 04/17/2025).

[56] The LHCb Collaboration. "Measurement of CP asymmetry in $B_s^0 \to D_s^{\pm} K^{\pm}$ decays". In: *LHCb-CONF-2023-004* (2023). URL: https://cds.cern.ch/record/2873713/files/LHCb-CONF-2023-004.pdf.

[57] The LHCb Collaboration. "Observation of Cabibbo-Suppressed Two-Body Hadronic Decays and Precision Mass Measurement of the Ω_c^0 Baryon". In: *Phys. Rev. Lett.* 132 (8 2024), p. 081802. DOI: 10.1103/PhysRevLett.132.081802. URL: https://link.aps.org/doi/10.1103/PhysRevLett.132.081802.

[58] M. Pivk and F. R. Le Diberder. "sPlot: A statistical tool to unfold data distributions". In: *Nucl. Instrum. Meth.* A555 (2005), pp. 356–369. DOI: 10.1016/j.nima.2005.08.106. arXiv: physics/0402083 [physics.data-an].

[59] M. Caporale. "First Measurement of Time-Dependent $\mathcal{CP}$ Violation with $B_s^0 \to \pi^+\pi^-$ Decays at LHCb". MA thesis. Università di Bologna, 2024.